CHALMERS
UNIVERSITY OF TECHNOLOGY

Indirect Pressure Measurement in Batteries and State Estimation of SoH

Internal Gas Pressure measurement in Li-ion Cells for SoH Estimation using Deep Neural Network

Master's Thesis in Mobility Engineering

ADITYA SUNKU

DEPARTMENT OF ELECTRICAL ENGINEERING

CHALMERS UNIVERSITY OF TECHNOLOGY
Göteborg, Sweden 2024
www.chalmers.se

MASTER'S THESIS IN MOBILITY ENGINEERING

Indirect Pressure Measurement in Batteries and State Estimation of SoH

ADITYA SUNKU

Department of Electrical Engineering
Chalmers University of Technology
Gothenburg, Sweden 2024

Indirect Pressure Measurement in Batteries and State Estimation of SoH
ADITYA SUNKU

Academic Supervisor: Torbjörn Thiringer & Kristian Bartholdsson Frenander, Department of Electrical Engineering

Industrial Supervisor: Farshad Abbasi, Manager Validation, Cell Development, Northvolt AB, Västerås, Sweden.

Examiner: Torbjörn Thiringer, Department of Electrical Engineering

Master's Thesis Report
Department of Electrical Engineering
Chalmers University of Technology
SE-412 96 Gothenburg
Sweden
Telephone +46 31 772 1000

Cover: Northvolt Prismatic cell for Volvo

Typeset in LaTeX
Gothenburg, Sweden 2024

Indirect Pressure Measurement in Batteries and State Estimation of SoH
ADITYA SUNKU
Department of Electrical Engineering
Chalmers University of Technology

Abstract

This thesis presents a new methodology for internal gas pressure measurement in Li-ion batteries to predict the State of Health of the battery. This is achieved by a simulation study, experimental testing of Li-ion batteries and a Deep Neural Network (DNN) model for state estimation. The primary motive of this thesis is to measure the internal gas pressure in Li-ion batteries in a non-invasive approach and to asses the battery health based on the amount of gas generated inside the cell over its life cycle. The traditional methods used in present day BMSs, use electrical parameters like voltage and current as input parameters to asses the states of a battery like State of Health (SoH), State of Charge (SoC). This study aims to take into consideration the mechanical parameters of the battery like internal gas pressure and cell temperature, for state estimation.

This Master Thesis deals with an in-operando, non-invasive pressure measurement of batteries. The internal gas pressure of the battery was monitored by capturing/measuring the strain developed on the battery cell lid. Uses this measured/predicted internal gas pressure as an input variable to the battery management system (BMS) for SoH estimation. Extensive cell testing was performed to capture the cell behaviour during cycling and measure the gas pressure developed inside the cell. This data was used as input parameters for the Deep Neural Network (DNN) model, developed to predict the State of Health (SoH) of the battery.

Through this study, a correlation between internal gas pressure and health indicators of batteries like Direct Current Internal Resistance (DCIR), Discharge Energy and & Charge Capacity of the battery was established. This correlation further aids in accurately predicting the State of Health (SoH) of the battery.

Keywords: Indirect gas pressure measurement, in-operando, gas pressure, strain, State of Health (SoH), BMS, Deep Neural Network (DNN), DCIR, Discharge Energy, Charge Capacity

Acknowledgements

The thesis work has been carried out at the Department of Electrical Engineering at Chalmers University of Technology, Sweden and Cell Development, Northvolt AB, Sweden.

I would like to express my gratitude to,

- Torbjörn Thiringer and Kristian Barthodlsson Frenander for their continuous support and guidance, regular technical reviews throughout the duration of my thesis.

- Farshad Abbasi and Moritz Schieder for giving me the opportunity to undertake my Master's Thesis at Northvolt.

- Farshad Abbasi for the all the help, technical guidance and continuous mentoring throughout my thesis. The valuable insights and suggestions provided throughout the thesis at various stages of the thesis was very helpful.

- The test teams at Safety and Environment & Performance and Life for their assistance and support in carrying out the tests which enabled me collect valuable data for my thesis.

Aditya Sunku
Gothenburg, August 15, 2024

List of Acronyms

Below is the list of acronyms that have been used throughout this thesis listed in alphabetical order:

BEV	Battery Electric Vehicle
BMS	Battery Management System
DCIR	Direct Current Internal Resistance
DNN	Deep Neural Network
ESS	Energy Storage Systems
EV	Electric Vehicle
FCEV	Fuel Cell Electric Vehicle
ISA	International Solar Alliance
LVDT	Linear Variable Differential Transducer
NN	Neural Network
PHEV	Plug-in Hybrid Electric Vehicle
QRL	Quality Reliability & Life
RNN	Recurrent Neural Network
SDG	Sustainable Development Goals
SEI	Solid Electrolyte Interphase
SoC	State of Charge
SoH	State of Health
VBT	Vent Burst Test/Tester

Contents

1

Introduction

Amidst a steep rise in global warming and the alarming effects of climate change, the clarion call of world leaders has been Net-Zero Emmissions. Pro-active measures are being taken by World leaders and their governments towards green energy transition. Policies of countries and corporates have shifted towards a greener and sustainable future abiding by the Sustainable Development Goals (SDGs) of the United Nations. Initiatives like the International Solar Alliance (ISA) proposed by India and France aim towards a greener and cleaner form of energy generation using solar power. Net Zero Emissions is not limited to energy generation, but also energy consumption. Major contributors to global air pollution apart from Industries are the automobile and transport sector that primarily operate on fossil fuels. Due to the efforts, policy driven changes and transition in the outlook of stakeholders, there is now a rapidly rising market for electric vehicles (EVs), primarily in the road transport sector. Figure 1.1 graphically depicts the rapid rise in the adoption of EVs in the automobile market. The EV market currently comprises of battery electric vehicles, plug-in hybrid vehicles and fuel cell electric vehicles with BEVs topping the market share and consumer preference.

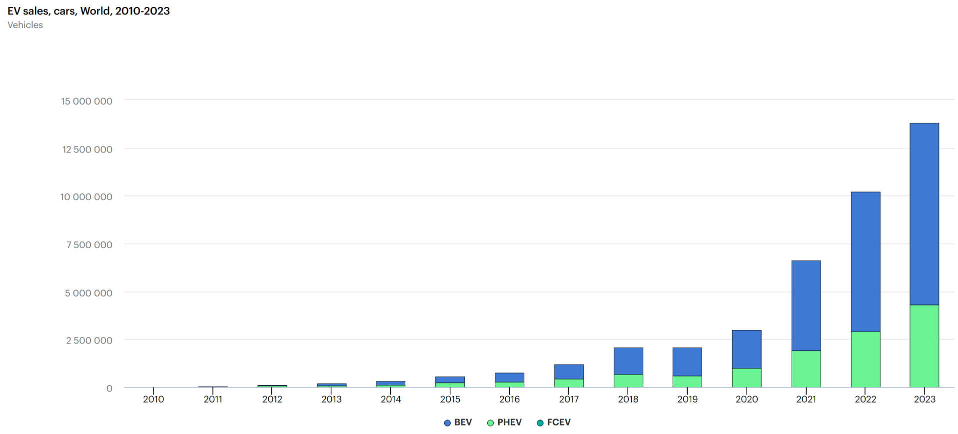

Figure 1.1: EV sales of cars in the World between 2010-2023

With increasing usage and adoption of EVs in the global market, the safety, design and monitoring of batteries becomes very crucial and integral. Batteries in the future will have many varied applications, be it EVs or energy storage systems. With constant upgrades and improvements made in different battery aspects such as cell formats, cell chemistry, energy density and various other aspects, it is critical to improve the quality, reliability and life (QRL) of the battery.

It is these parameters that determine the future performance and operational application of the battery. With the aim of developing better methods to monitor the battery State of Health (SoH), accurate and precise real-time measurement of the battery health is necessary.

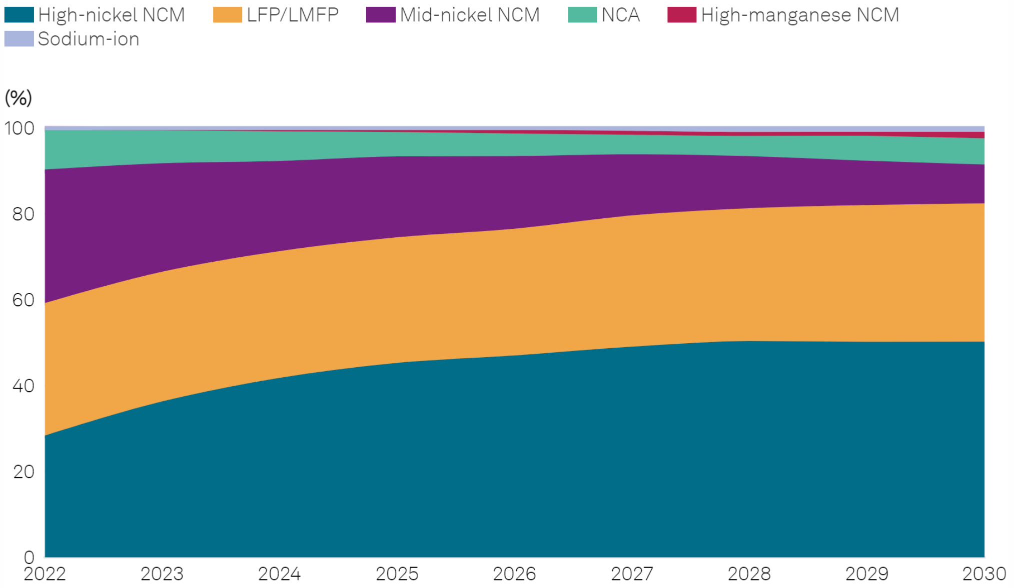

Data compiled October 2023.
LV = light vehicle; GWh = gigawatt-hour; NCM = lithium, nickel, cobalt, manganese; LFP = lithium, iron, phosphate; LMFP = lithium, manganese, iron, phosphate; NCA = lithium, nickel, cobalt, aluminum oxide.
Source: S&P Global Mobility, AutoTechInsight, High Voltage Battery forecast.
© 2024 S&P Global.

Figure 1.2: High voltage battery forecast based on Battery Chemistry

The Figure 1.2 provides a pictorial representation of the emerging battery chemistry in the electric battery market. With ever increasing demands in the battery energy density and cycle life, it becomes very important to constantly monitor and understand various battery parameters of different battery chemistry.

1.1 Problem Background

Northvolt is committed to developing the world's greenest batteries and contribute to the green energy transition that is currently underway in Europe. With the vision to accelerate the transition to a decarbonized future, by supplying sustainable, high quality battery cells and systems Northvolt is developing state of the art lithium-ion and Na-ion battery cells to propel the transition. The current focus at Northvolt is on both the prismatic and cylindrical formats with various chemistries and requirements.The batteries made by Northvolt are used by OEMs in their battery pack and by companies for ESS. The batteries used in the commercial applications are controlled and monitored by the BMS. The BMS plays an integral role in the operation and usage of battery packs both in the automotive and ESS applications. The existing BMSs, use voltage, current and temperature as input parameters to estimate other important parameters like SoH, SoC, capacity fade, etc. We at

Northvolt would like to develop alternative methods to understand and capture the mechanical behaviour of the cell and provide mechanical parameters as input to the BMS for a more accurate and efficient state estiamtion of various battery parameters. With this motive, we decided to understand various parameters in the cell that could help us interpret the cell behaviour and health. Gas pressure generated in the cell during its life-cycle was an important variable less discovered and understood in terms of state estiamtion of batteries. For this, we

1.2 Objectives

- To develop a non-invasive method for gas pressure measurement in Li-ion cells, where we take advantage of various geometrical features of the cell and their respective corresponding response to change in internal gas pressure.
- Use strain gauges to capture the change in gas pressure inside the cell. Use these strain gauge readings in terms of μm/m. These strain readings will be used as input to the NN algorithm to predict or accurately estimate the gas pressure inside the Li-ion cell.
- Using NN, achieve the state estimation of State of Health of the battery. Aim is to estimate the state of health (SoH) of the Li-ion battery using mechanical parameters like strain and temperature.

1.3 Specifications of the Issue under Investigation

The current thesis work would address the following:

- Developing alternative methods to accurately measure gas pressure inside the cell without using the gas pressure sensor.
- Enable real-time accurate pressure measurement and health of the battery using modern methods and tools like Artificial Neural Networks for state estimation
- Use the newly developed method, to compliment the existing BMS in further improving the capabilty of the BMS for better monitoring and usage of the battery cells in the battery pack.

2

Theory

Evolution of Mobility and the modes of transport have been an integral part of human evolution. From the invention of the wheel to horse driven chariots used in the ancient civilizations as shown in Figure 2.1 to the first ever gasoline powered automobile made in 1885 as shown in Figure 2.2 to the present day modes of transport powered by clean energy. This transition has transformed the manner in which we travel.

Figure 2.1: Horse Driven Chariots

Figure 2.2: Benz Patent Motorvagen

The transition from fossil fuels to green energy has facilitated the development of alternatives to fossil fuel like hydrogen, bio-gas, bio-fuels, electrical energy stored in batteries. Conventional vehicles were powered by internal combustion engines, which burnt fossil fuel, to release energy to propel the vehicles. With the rapid adoption of battery powered EVs gaining a huge market share of the transport sector, it is very important to design batteries that meet the demanding driving cycles and profiles of the current day transport sector. With increasing usage and adoption of EVs in the global market, the safety, design and monitoring of batteries becomes very crucial and integral. Batteries in the future will have many varied applications, be it EVs or energy storage systems. Combining modern technology like artificial intelligence and machine learning with state of the art data acquisition systems, it is important that we focus on the overall development of the battery which is summed up by the 5 point parameters. Based on our application and requirement, it is very essential to strike an optimal balance among the 5 parameters : Cost, Life, Charge Rate, Power and Energy Density.

2.1 Lithium - Ion Batteries

A Battery cell is a device that stores electrical energy and releases this stored energy when required. A Battery cell consists of two electrodes, an anode and cathode, a separator film that prevents the short-circuiting of the cell which could arise due to contact between the anode and cathode sheets. The anode, cathode sheets and the separator film constitute the jelly roll of the cell. This jelly roll is immersed in an electrolyte. The electrolyte enables the flow of charge between the anode and cathode sheets during charging and discharging. The jelly roll and electrolyte are contained in outer casings known as cell cans and are covered by cell lids. The lids are provided with vents, which open and release the pressure caused due to gas generation in the cell in case of failure or extreme cycling conditions.

Various steps are involved in the manufacturing of batteries. Once the aging and formation of the cells are done, they are ready to be used for their respective applications (in our case automotive and energy storage systems). A cell undergoes multiple charge and discharge cycles over its lifetime. During charging the lithium ions gain electrons at the graphite anode and Li ions are reduced to Lithium intercalated into the graphite anode, forming a lithium-carbon alloy with graphite, thus resulting in swelling (increase in thickness), in the direction of the jelly roll thickness. During discharge, some of the intercalated lithium dissolves and lithium loses electrons to form lithium ions and emerges from the graphite layer. This results in a decrease in the swelling force developed in the cell, resulting in a decrease in the cell thickness.

In the first charge-discharge cycle, the SEI film layer is formed on the anode sheets. On consecutive charge-discharge cycles, the SEI layer breaks down and a new SEI layer form. One of the major contributors for swelling force generation in the cells is this continuous growth and decay of the SEI and lithium dendrites during charging and discharging over the lifetime of the cell. During discharge, lithium near the anode preferentially, undergoes oxidative desorption because of large currents, resulting in fracture of dendritic lithium. This forms dead lithium in the cell. Therefore, swelling force in lithium-ion batteries tend to increase gradually with the progress of the charge-discharge cycle. In some cases, the cathode particles can crack during charging and discharging cycle, because of dislocation defects. When particles break, rigorous oxidation decomposition of the electrolyte takes place at the cathode surface, resulting in larger swelling force development. Decomposition of the electrolyte also leads to gas generation within the cell. This generated gas also contributes to the overall swelling force developed in the cell. The oxidation of the electrolyte at the cathode surface produces $CO_2$and reduction of the electrolyte at the anode surface produces gases like C_2H_4 and CH_4.

2.1.1 Battery Cell Terminologies

1. ***State of Charge (SoC)*:** SoC is the ratio of the remaining charge in a battery at any given instant, with respect to the maximum capacity of the battery. It is a very important parameter that describes the present charge stored in the

battery. SoC is an important parameter that is monitored by the BMS. SoC is expressed in %.

2. ***Terminal Voltage (V)*****:** The voltage between the terminals of a battery with a load applied. The terminal voltage varies with SoC.
3. ***Open-Circuit Voltage (OCV)*****:** The voltage between the terminals of the cell with no load applied. The open-circuit voltage depends on the SoC.
4. ***Nominal Voltage (V)*****:** Nominal Voltage is the reference or reported voltage of the battery. It is often referred to as the 'normal' voltage of the battery.
5. ***Cut-off Voltage (V)*****:** It is the minimum permissible voltage of a battery. It is not a good practice to go below cut-off voltage. The cut-off voltage often is used to describe the empty state of the battery.
6. ***Internal Resistance(Ω)*****:** It is the internal resistance of the battery. It depends on many factors. The jelly roll stacking, the chemical reactions, gas generation and many other factors result in a particular internal resistance. As the cell ages and as it cycles over a period of time, the internal resistance (DCIR) of the cell increases. As the internal resistance of the cell increases its capacity decreases almost in a proportional manner. The DCIR is dependent on the SoC of the battery.
7. ***Depth of Discharge (DoD) (%)*****:** Depth of discharge can be defined as the percentage of battery capacity expressed as a percentage of the maximum capacity of the battery. Often, it is considered that a DoD of 80% is referred to as deep discharge.
8. ***Capacity (Ah)*****:** The coulometric capacity, the total Amp-hours available when the battery is discharged at a certain discharge current (specified as a C-rate) from 100% state-of-charge to the cut-off voltage.
9. ***Energy (Wh)*****:** The energy stored or available in a battery is the total Watt-hours available when the battery is discharged at a certain discharge current (specified as a C-rate) from 100% state-of-charge to the cut-off voltage. Energy is calculated by multiplying the discharge power (in Watts) by the discharge time (in hours). As the C-rate increases, the energy decreases.
10. ***Discharge Capacity (Ah)*****:** It is the quantity of charge removed from a cell as it is discharged at a constant rate from a fully charged state until its loaded terminal voltage is reached. The Discharge Capacity generally decays gradually over time as the cell ages and degrades.

2.1.2 Parts and Assembly of Batteries

Every Li-ion battery cell, irrespective of the format (pouch, cylindrical or prismatic) consists of two electrodes (anode & cathode) and a separator which separates the electrodes from each other. The electrodes need to be manufactured based on the respective cell's chemistry. Irrespective of the cell type or cell format, production of cells can be broadly classified in 3 process steps:

- Electrode Manufacturing
- Cell Assembly
- Cell Finishing

Electrode manufacturing is a very important step as it involves the production of the cell's anodes and cathodes, which need to be of high quality to enhance and sustain the battery performance. The first step in electrode manufacturing is production of slurry. The active material, conductive additives and binder are dry mixed. This is followed by a process called dispersing, where a solvent is added to the dry mix, in order to disperse and homogenize the dry mix to form the slurry. Quality features such as homogeneity of the slurry, particle size, purity (amount of foreign particles) and viscosity of the slurry are very important features or quality control parameters that determine the quality of the slurry produced. It should be taken into account that the mixing and dispersing sequence must be strictly followed as per the recipe and the specified temperature must be maintained while mixing. It is advisable to carry out the mixing process in the atmosphere of a protective gas/vacuum environment to avoid gas inclusions.

Electrode coating is the next major step in electrode manufacturing. The foil is coated with slurry tools. The coating on the foil can happen sequentially on each side of the foil or simultaneously on both sides of the foil. Figure 2.3 shows a schematic of an electrode coating machine.

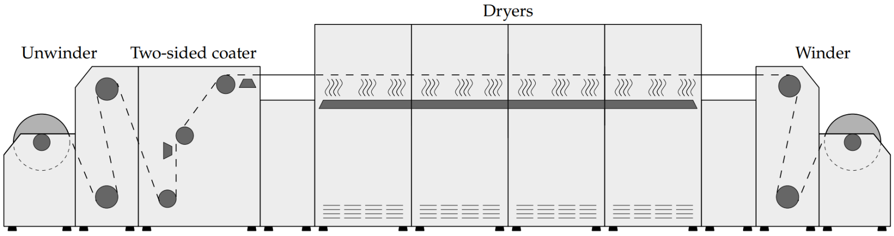

Figure 2.3: Schematic of Electrode Coating Machine

The first step involves unwinding the foil (aluminium foil for cathode and copper foil for anode), followed by a simultaneous coating of the slurry on both sides of the foil. Quality features such as coating thickness accuracy, that is homogeneity in and across the direction of coating, ensure surface quality by checking for blowholes and particles. It is important that there is good adhesion between the coating and substrate. Once the active material is applied on the foils, the active material is dried in a continuous process. During the drying process, the solvent is removed from the active material by heat supply. Methods like infrared drying or laser drying can be used for this purpose. The foil/electrode sheets are sent into the dryer with different temperature zones for different temperature profiles during the frying process. coated foil is transported across the drying chamber via rollers (in case of single side coated) or floatation air streams (in case of double sided coating). Foil pretension and temperature profile are parameters that could influence the quality of the produced electrode. Quality features like adhesion between coating and substrate, residual humidity and surface finish (look out for cracks/inclusions) must be monitored for improved electrode quality. Figure 2.4 depicts a pictorial representation of double side coated electrodes.

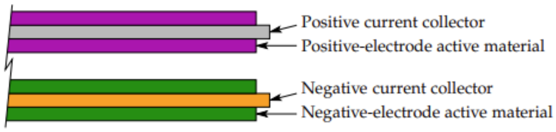

Figure 2.4: Double coated electrode foil

Once the foil are coated, they are wound into rolls and transported to the the next stage called calendaring and slitting. During the calendaring process, the electrode foil is unwound and the the copper or aluminium electrode foil coated on both sides is initially statically discharged and the electrode foil is cleaned by brushes or air flow.

Electrode foil is then compressed by a pair of rotating rollers where the material on the foil is compacted. The pair of rollers apply a precisely defined line of pressure on the electrode foil. This line of pressure defines the porosity of the coated electrode foil, which influences the subsequent wetting properties of the electrodes when the electrolyte is introduced, which then would effect the energy density of the cell. If the line pressure is too high, it could lead to the formation of stress cracks and other irregularities in the electrode foil. Upon calendaring, the thickness of the outgoing electrode foil is constantly monitored to ensure very good quality. The next process involves slitting of the calendared mother rolls of electrode foil.

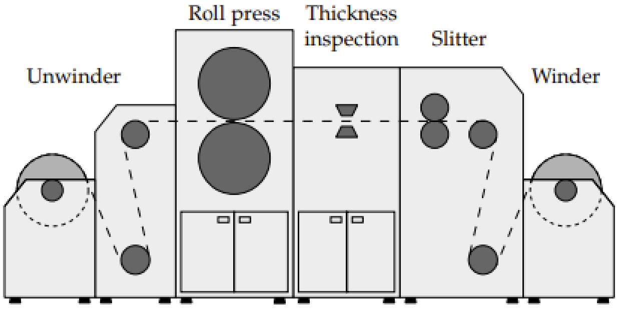

Figure 2.5: Schematic of Calendaring and Slitting

Slitting is a separation process in which the wider electrode foil roll (mother roll), is divided into several smaller electrode coils also known as daughter rolls. The mother roll is slit along its length to produce daughter rolls with width depending on the format, type and dimensions of the cell for which the electrode foil will be used. Physical rolling knives or more advanced methods like laser slitting may be used for the cutting process.The daughter rolls are then cleaned by brushes or suction and rewound after the cutting and cleaning process. A schematic of the calendaring and slitting machine is showed in Figure 2.5.

The daughter electrode foil rolls undergo winding for the production of prismatic and cylindrical cells, after vacuum drying of the daughter electrode rolls. The electrode foils (both the anode and cathode foils) and the separator foil are wound around a rotating flat mandrel, in case of prismatic cells and a rotating pin or circular mandrel in case of cylindrical cells. In some cases for prismatic cells, the electrode foil is cut and stacked in a particular sequence with the separator foil. In case of stacked method, the cathode and electrode foil is alternately stacked between each layer of the separator sheet.

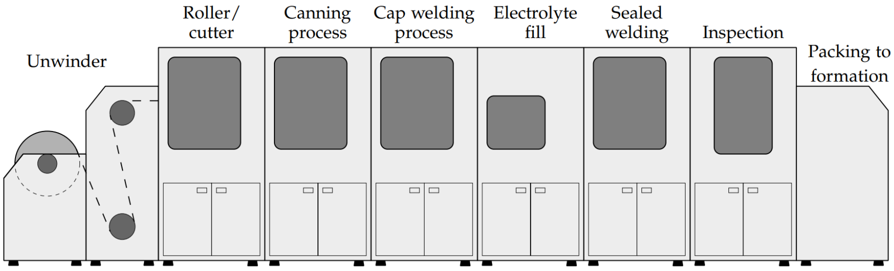

Figure 2.6: Schematic of Cell Assembly

The wound/stacked electrode foil-separator bundle is called a Jelly Roll. The next step in the cell manufacturing is the canning process. The jelly roll is inserted into a metallic housing, generally made of steel or aluminium (both for prismatic or cylindrical cells). The tabs of the anode and cathode electrode foils of the jelly roll are grouped and ultrasonically welded to their respective current collectors. The current collectors are a part of the battery lid. These current collectors are connected to the respective anode and cathode terminals of the cell. The jelly rolls are also wrapped with an insulation foil, in order to protect the jelly roll during the insertion of the jelly roll into the metal casing. The insulation foil also prevents the electrical contact between the jelly roll and cell housing. Once the jelly roll is inserted into the cell housing, the lid and metal housing of the cell is sealed by a laser welding process. The cell at this stage is called a dummy cell (due to the absence of the electrolyte). The next step in the battery manufacturing process is the electrolyte filling. With the help of a high precision dosing needle, the electrolyte is filled in the the cell through the electrolyte filling hole under vacuum (in order to prevent any trapped air bubbles that may arise). The next step is for the wetting of the jelly roll with the electrolyte. Wetting is achieved by the application of a pressure onto the cell, which then facilitates wetting, due to the capillary action/effect. The cells undergo evacuation and partial filling several times based on the cell design and the manufacturer's requirement. Once the filling is done, the electrolyte filling hole (in case of prismatic cells) is sealed using laser welding. Some quality control parameters for the electrolyte filling process could be distribution accuracy of the electrolyte within the cell and quantity of the electrolyte. Final inspection is carried out on the cell before it moves to the next stage of Formation and Ageing before packaging. The above mentioned process can be seen in a simplified pictorial representation as shown in Figure 2.6.

2.1.3 Working Principle - Batteries

During the discharge process of a battery, the negative electrode releases electrons into the external circuit, a process known as oxidation. Oxidation involves the loss of electrons, leading to an increase in the oxidation state, meaning the species becomes more positively charged. Conversely, during charging, the negative electrode gains electrons from the external circuit, undergoing reduction, which decreases the oxidation state, making the species more negatively charged. The reactions that occur within an electro-chemical cell are often referred to as redox (reduction-oxidation) reactions. The negative electrode is typically referred to as the anode. However, the term "anode" technically applies to the electrode where oxidation occurs, so during discharge, the negative electrode is the anode. When the cell is being charged, the negative electrode becomes the cathode, since reduction is taking place. To avoid confusion, this work will use the term "negative electrode" instead of "anode." The positive electrode in an electro-chemical cell is usually made from materials such as metallic oxides, sulfides, or oxygen. For instance, in a lead-acid battery, the positive electrode is composed of lead dioxide, typically formed from a lead-oxide paste applied to a lead alloy grid. During discharge, the positive electrode receives electrons from the external circuit, a process known as reduction. Conversely, during charging, it loses electrons and undergoes oxidation. While the positive electrode is commonly called the cathode, this term is technically accurate only during discharge, when reduction occurs. When the cell is being charged, the positive electrode becomes the anode. To minimize confusion, this text will consistently refer to it as the "positive electrode." The electrolyte in the cell acts as an ionic conductor, facilitating the transfer of ions between the electrodes. Most often, the electrolyte is a liquid solvent containing dissolved substances (the solute) that enable ionic conductivity, although solid polymer electrolytes are also possible. During discharge, positively charged ions (cations) move through the electrolyte toward the positive electrode, while negatively charged ions (anions) (if present) move toward the negative electrode. During charging, the ion movement reverses: cations head toward the negative electrode and anions toward the positive electrode.

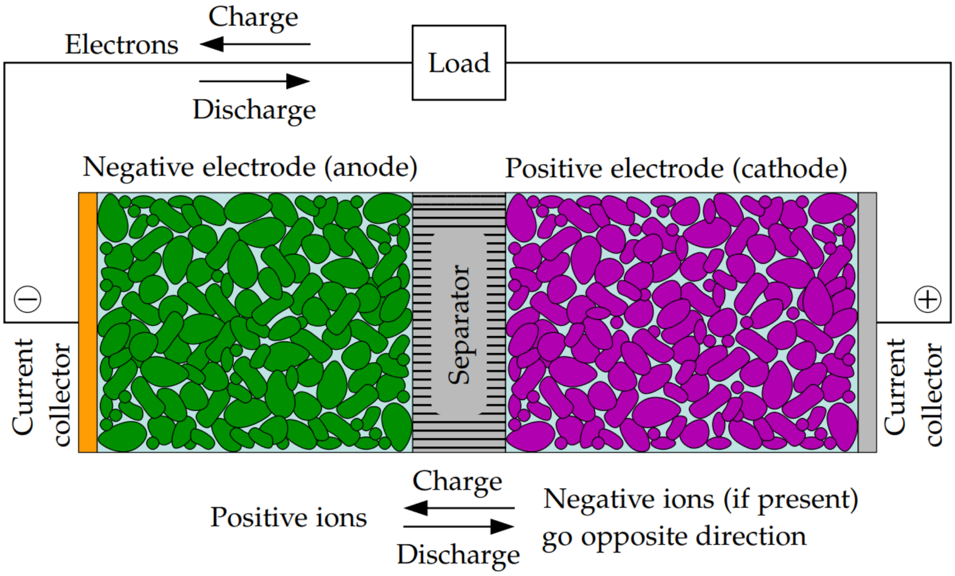

Figure 2.7: Schematic of Li-ion Cell

2.1.4 Aging of Batteries

- ROOT CAUSE
  - Time
  - High Temperature
  - High SoC
  - Low SoC
  - High Current
  - Low Temperature
  - Energy Cycles
- DEGRADATION MODE
  - SEI Growth
  - Electrolyte Decomposition
  - SEI Decomposition
  - Binder Decomposition
  - Transition Metal Dissolution/Dendrite Formation
  - Graphite Exfoliation
  - Structural Disordering
  - Current Collector Dissolution
  - Li^+ Plating
  - Loss of Electrical Contact
  - Particle Cracking and Island Formation
- DEGRADATION MECHANISM
  - Loss of Cycleable Li
  - Loss of Active Anode Material
  - Loss of Active Cathode Material
  - Reduced Kinetics
  - Increased Electrical Resistance
- MEASUREABLE EFFECT
  - Capacity Loss
  - Resistance Rise

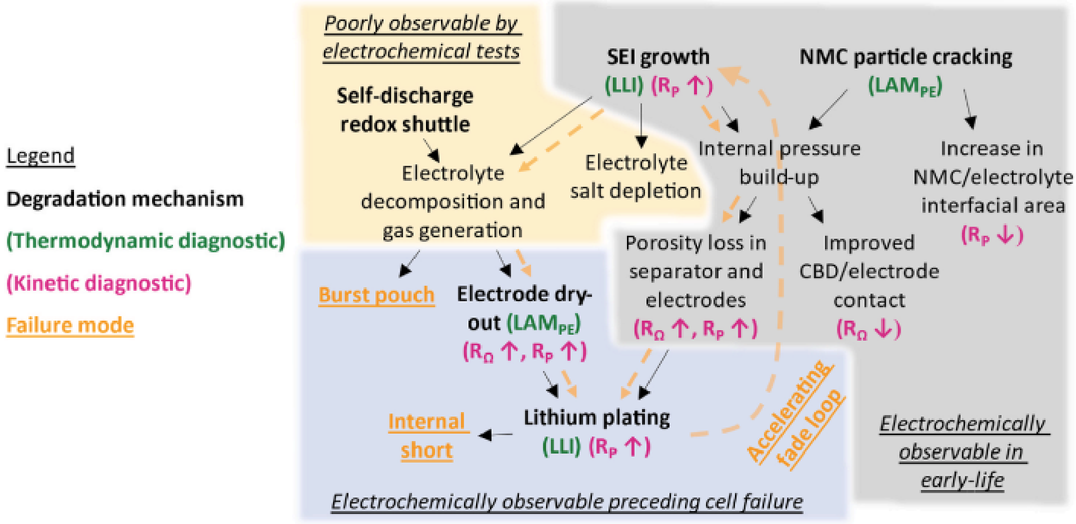

Figure 2.8: Degradation mechanisms in NMC cell

The Figure 2.8 gives a better picture and understanding of the degradation mechanisms in a typical NMC cell.
During cycling, as lithium ion cells age, pressure inside the cell eventually increases. This pressure developed inside the cell can be categorized into two categories:

- Mechanical Pressure (Swelling)
- Gas Pressure

The mechanical swelling and the gas pressure developed in the cell during cycling, are an indication of the aging of the batteries. In a lithium ion cell, the major contributor to the overall swelling of the cells is due to the mechanical pressure cause by the jelly roll. The gas pressure also contribute to swelling but the contribution from gases is minor and more towards the lid of the cell.

2.1.5 Mechanical Pressure (Swelling)

A lithium-ion cell undergoes multiple charge and discharge cycles throughout its lifetime. During charging, lithium ions gain electrons at the graphite anode, becoming reduced and intercalating into the graphite to form a lithium-carbon alloy, which causes the anode to swell, increasing the cell's thickness along the jelly roll. During discharge, some of the intercalated lithium is released, losing electrons and emerging from the graphite as lithium ions. This leads to a reduction in the swelling force, which decreases the cell's thickness. In the initial charge-discharge cycle, a SEI layer forms on the anode. During subsequent cycles, this SEI layer degrades and reforms. The continuous formation and breakdown of the SEI, along with lithium dendrite growth during charging and discharging, contributes significantly to the swelling force in the cell over time.

During discharge, the lithium near the anode undergoes oxidative desorption, especially under high currents, causing dendritic lithium to fracture and form "dead lithium" in the cell. As a result, the swelling force in lithium-ion batteries tends to increase gradually with repeated charge-discharge cycles, as shown in Figure 2.9. Figure 2.9, illustrates the trend of swelling force, showing that as the cell continues to cycle, the swelling force within the cell gradually increases over time. This is represented by the black line connecting the peaks of the swelling force generated during consecutive charge-discharge cycles. In some cases, cathode particles may crack due to dislocation defects during these cycles. When this happens, oxidation decomposition of the electrolyte occurs more aggressively at the cathode surface, further increasing the swelling force.The swelling force in a cell is directly related to the number of electrode sheets or windings in the jelly roll. Increasing the number of windings (and thus the jelly roll thickness) boosts the battery's capacity and energy density but also leads to greater swelling force development within the cell.

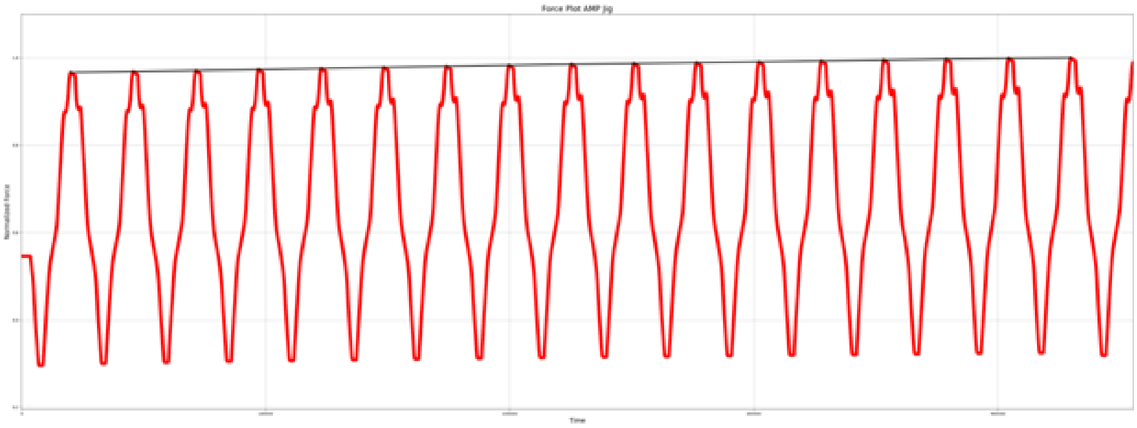

Figure 2.9: Swelling Force Developed in a Cell under cycling

2.1.6 Gas Pressure

As the Li-ion cell undergoes cycling (charging and discharging), the cell begins to age. One of the main by-products of aging is gas generation. As the cell ages, the internal gas pressure inside the cell tends to increase. The internal gas pressure is a very important parameter that varies with respect to the cell cycling conditions, cell heating and the dynamic load conditions of the cell. A Li-ion cell being an electro-chemical device, undergoes chemical reactions during charging and discharging. Carbon monoxide (CO), carbon dioxide (CO_2) and ethylene (C_2H_4) are the primary gases that are generated in Li-ion batteries. Other constituents of gas developed in the cell could include hydrogen (H_2), methane (CH_4), ethane (C_2H_6) and very small traces of nitrogen (N_2). As a result of these chemical reactions within the cell, a small amount of residual gas is collected inside the cell body and accumulates over the life-cycle of the cell. This gradual build-up of gases inside the cell, could then be a promising indicator of the battery health and the performance of the battery.

The internal gas pressure developed inside the cell is expected to increase according to the ideal gas equation:

$$P \cdot V = n \cdot R \cdot T \tag{2.1}$$

where:

- P is the absolute pressure of gas,
- V is the gas volume,
- n is the number of moles of the gas,
- T is the temperature of the gas,
- R is the universal gas constant 8.3145 J/mol K

The irreversible gas pressure build-up in the cell, begins to accumulate over a period of time and this accumulated gas is a good indicator of the cell health. The gas pressure has a cyclical behaviour during cycling of the cells. The gas pressure is dependent on the SoC level of the cell. And this dependence of the gas pressure with SoC was useful in better understanding the battery behaviour.

2.2 Strain Gauges

One of the early inventors of the strain gauge was Prof. Arthur C Ruge of Caltech, working in the field of engineering seismology and the effect of earthquakes on mechanical structures. The first developed version of the present day modern strain gauges was a simple setup, made from a thin metallic wire from a potentiometer. This simple setup was used to understand and study the mechanical loading of mechanical structures. The change in the mechanical loading resulted in a corresponding change in the electrical resistance of the thin wire and this in-turn changed the voltage drop in the wire and was measured by a simple bridge circuit. The first strain gauge developed by Prof. Arthur C Ruge can be seen in Figure 2.10

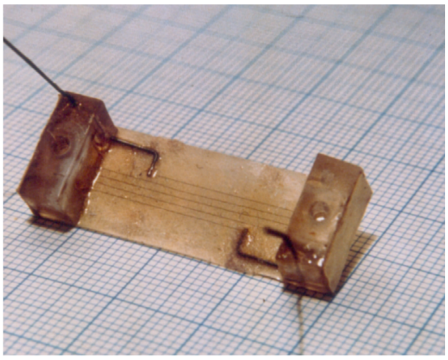

Figure 2.10: Ruge's strain gauge from 1938

The first flat grid strain gauges was developed in Sweden by Gustafsson as shown in Figure 2.11. The present day strain gauges and the strain gauges used in this research are advanced versions of the flat grid strain gauges developed by Gustafsson.

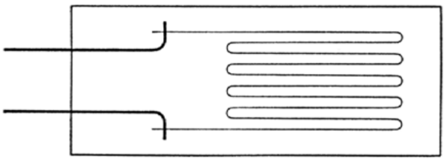

Figure 2.11: Schematic of Gustafsson's Flat grid SG

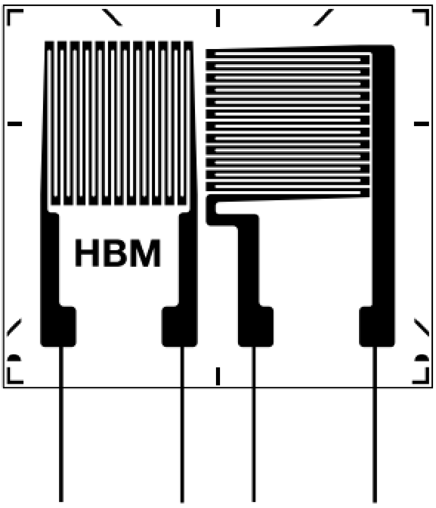

Figure 2.12: Bi-directional Strain Gauges - Drawing

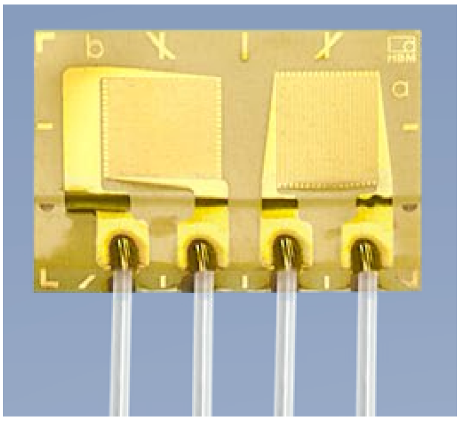

Figure 2.13: Bi-directional Strain Gauges

2.2.1 Working Principle

The fundamental working principle of strain gauges is the conversion of strain (mechanical deformations) into an electrical signal. Strain is the mechanical quantity to be measured. Changes in strain, produce a corresponding change in the electrical resistance in the strain gauge, resulting in a change of the output voltage from the Wheatstone circuit. The Wheatstone Bridge circuit is used for compensation of unwanted effects on the strain gauges like the effect of temperature. As shown in Figure 2.12 & Figure 2.13, the strain gauges have a grid arrangement.

The strain gauges measure the mechanical strain that occurs along the longitudinal direction of the measuring grid. That mechanical strain produces a change in the electrical resistance of the measuring grid of the strain gauges, resulting in a measurable imbalance to the Wheatstone bridge circuit, to which the strain gauge is connected. The strain gauges are not significantly affected by the mechanical strain that may arise in the transverse direction of the measuring grid and hence it can be neglected.

$$\text{Strain} = \frac{\text{Change in dimension}}{\text{Original dimension}} \tag{2.2}$$

Theoretically strain is defined in (2.2).

$$\varepsilon = \frac{\Delta L}{L_0} \tag{2.3}$$

We generally consider the dimension to be length and (2.2) can then be symbolically represented as shown in (2.3) where ΔL is the change in length and L_0 is the original length.

$$\mathcal{E}_{SG} = \frac{1}{x_2 - x_1} \int_{x_1}^{x_2} \mathcal{E}(x)\, dx \tag{2.4}$$

$\varepsilon_{\mathrm{SG}}$ - Magnitude of strain measured by strain gauge and is converted to change in electrical resistance x_1 and x_2 - The longitudinal coordinates of the active lengths of the measuring grid

In reality, the strain gauge detects the effective strain developed at the surface of measurement as defined in (2.4) If the strain gradients occur in the measurement object along the length/orientation of the measuring grid of the strain gauge, then the strain gauge behaves like an integrating measuring element and measures the mean of the strain developed in the region of the active length of the measuring grid, according to the law of averages in integral calculation as shown in Figure 2.14. This integrating characteristic/feature of strain gauges is a significant property to take into consideration in the selection of the appropriate dimensions of the strain gauge length (active grid length of the strain gauge).

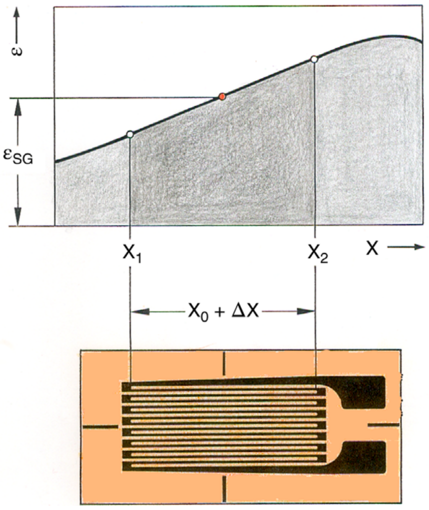

Figure 2.14: Law of averages in integral calculation

2.2.2 Types of Strain Gauges

Different types of strain gauges can be used for measuring strain arising in specimens based on the application and type of loading causing the strain to develop in the specimen. A schematic of various types of strain gauges can be seen in the Figure 2.15.

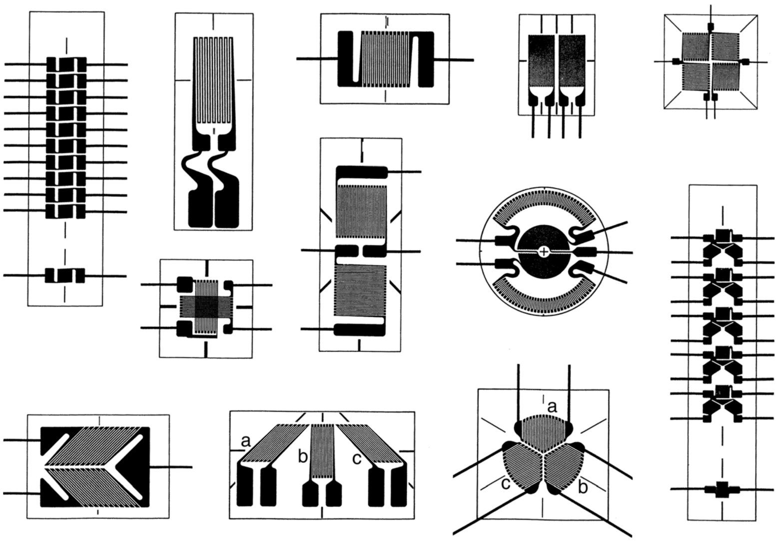

Figure 2.15: Schematic of various types of Strain Gauges

2.2.3 Alternatives to Strain Gauges

Strain gauges as described above are very user friendly and simple to operate and use. Strain gauges have a measuring grid made of a particular metal wire. When any deformations or strain is detected in the specimen, this results in a change in the resistance of the measuring grid and this is corresponding output voltage from the strain gauge measuring grid is converted to strain. Temperature compensation plays a very big role in affecting the measurements made by the strain gauge. Strain Gauges also require regular calibration for accurate measurements over a long period of time. An optical fiber on the other hand is not temperature dependent and can be used in any kind of working environment. The FBG sensor is stuck to the cell as shown in Figure 2.16. Light is passed through the FBG sensor during the measurement process. as the strain is developed in the cell, the FBG sensor expands or contracts accordingly. This results in the loss of a particular spectrum of the light that is incident upon the FBG sensor. The light emitted out by the FBG sensor is does not contain a particular spectrum of light or there can be a frequency drift. The extent of the drift or the spectrum of light missing from the light leaving the FBG sensor is used to determine the strain developed in the cell. Figure 2.17, gives a pictorial representation of how the FBG sensor can be used for strain measurement.

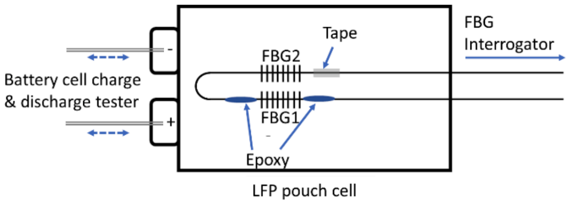

Figure 2.16: Schematic of FBG sensor placement on Pouch Cell

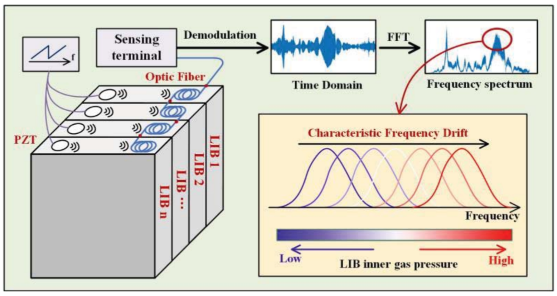

Figure 2.17: Schematic of FBG based Li-ion cell monitoring

2.3 State Estimation

Parameters like Voltage, Current, State of Charge, Energy and other such parameters can be calculated using sensors of available primary data like voltage, current and resistance. But there are certain parameters, that cannot be measured directly with the help of sensors or any devices. such parameters can be obtained by state estimation. State estimation can be used or employed to determine the health of the battery, state of charge, remaining useful life (RUL) of the battery and many more. There are 3 primary approaches for state estimation. They are:

- Adaptive Filter Methods
  - Kalman Filter
  - Particle Filter
  - Improved Particle Filter
- Machine Learning
  - Neural Network
  - Deep Learning
  - Support Vector Machines
- Stochastic Process Methods
  - Bayesian Estimation
  - Gaussian Process Regression
  - Wiener Process Model

In this report we will discuss a few of the above mentioned methods. The discussion will revolve around machine learning methods and adaptive filter methods, with a discussion on each of the above specified methods, their advantages, disadvantages and an argument to support the preference of a particular method adopted in this thesis over the others.

2.3.1 Neural Network

A Neural Network (NN) is a computational model designed to simulate the way biological neurons work in the brain. It consists of layers of interconnected nodes or neurons, which transform input data to output predictions by learning from the patterns and trend of the input data provided to the neural network. A neural network in general comprises of 3 layers: Input Layer, Hidden Layers and Output Layer, as shown in Figure 2.17.

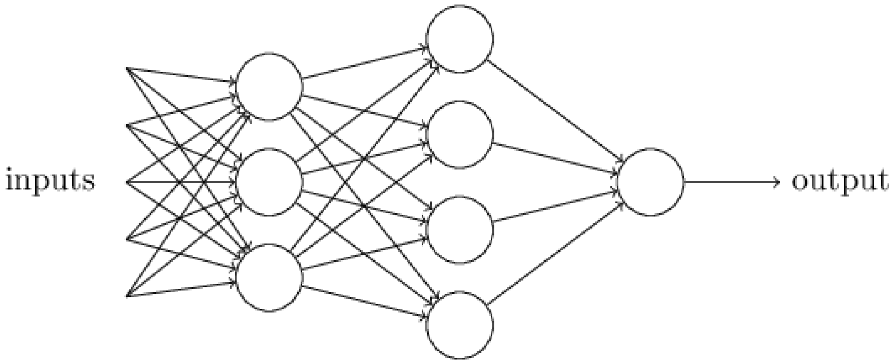

Figure 2.18: Pictorial representation of a basic Neural Network

- **Input Layer**

  The input layer is the first layer in a neural network and is responsible for receiving the input data. Each node/neuron in the input layer represents a feature or attribute of the data. The number of nodes/neurons depends on the number of features or input parameters provided as input to the neural network.

- **Hidden Layers**

  Layers between the input layers and output layer is called hidden layer or dense layer. Hidden layers perform computations and transformations on the input data. They process the data by applying weights, biases, and activation functions to the input data. Each hidden layer contains neurons that perform weighted sums on inputs and pass them through an activation function to introduce non-linearity. The hidden layers allow the network to learn complex patterns and relationships in the input data provided. When a neural network has multiple hidden layers, it's referred to as a deep neural network. Each neuron takes the inputs from the previous layer, multiplies them by weights (which are learned), adds a bias term, and applies an activation function to the result to determine whether to activate the neuron or not. These are the parameters that the network learns during training. They determine the strength of the connection between neurons in different layers. If the weight is high, it means that the neuron's output significantly influences the next layer. A bias is an additional parameter that allows the model to fit the data better by shifting the activation function. It's added to the input before passing it through the activation function. After the neuron performs a weighted sum of its inputs, it applies an activation function. This function introduces non-linearity into the network, enabling it to model complex patterns. Some of the common types of activation functions are ReLU, Sigmoid, Tanh and Linear.

- **Optimization Algorithm**

  An optimization algorithm in the context of neural networks is a method used to adjust the parameters (weights and biases) of the network to minimize the loss function (or cost function). The goal is to improve the network's performance by finding the set of parameters that yield the lowest possible error on the training data. The main purpose of the optimization algorithms is to iteratively update the model's parameters towards the direction of lower errors/loss. This is achieved with the concept of gradient descent. The optimizer computes the loss using loss functions as shown below. The gradient of the loss function is computed for each parameter. The gradient supports the optimizer to minimize the losses. The optimizer uses a common formula for updating the weights as represented by the equation below:

  $$w_{\text{new}} = w_{\text{old}} - \eta \frac{\partial L}{\partial w} \tag{2.5}$$

  where:
  - w_{new} is the updated weight,
  - w_{old} is the current weight before the update,
  - η is the learning rate, a hyperparameter that controls the step size of the update,
  - $\frac{\partial L}{\partial w}$ is the gradient of the loss function L with respect to the weight w.

  (2.5) shows that we update the weight by moving it in the direction opposite to the gradient (to minimize the loss). The size of the update is controlled by the learning rate η. There are various optimization algorithms that can be used like Gradient Descent, Stochastic Gradient Descent, Adam, Momentum and many other algorithms.

- **Learning Rate**

  Controls how large a step the algorithm takes when updating the weights. A small learning rate leads to slow convergence, while a large learning rate can cause the model to overshoot and diverge. The optimal learning rate for the neural network model, can be identified by an iterative process based on the desired convergence.

- **Loss Functions**

  There are generally three main types of loss functions used in neural networks, they are : MAE, MSE and MAPE.

  Mean Absolute Error (MAE) is a commonly used loss function in deep neural networks, especially for regression tasks. It measures the average magnitude of the errors between predicted values $\hat{y}_i$ and the actual target values y_i without considering their direction.

$$\mathrm{MAE} = \frac{1}{n}\sum_{i=1}^{n} |\hat{y}_i - y_i| \times 100\% \tag{2.6}$$

MSE (Mean Squared Error) is defined as the average of the squared differences between the predicted values $\hat{y}_i$ and the true values y_i. The squared term in MSE means that larger errors contribute significantly more to the loss than smaller ones. The gradient of MSE with respect to the model's parameters is continuous and smooth, which often leads to more stable convergence during training.

$$\mathrm{MSE} = \frac{1}{n}\sum_{i=1}^{n} (\hat{y}_i - y_i)^2 \times 100\% \tag{2.7}$$

Mean Absolute Percentage Error (MAPE) is a loss function often used in regression tasks, particularly when the goal is to express the prediction error as a percentage of the predicted values $\hat{y}_i$ and the actual values y_i. MAPE is especially useful in deep neural networks when the focus is on the relative error rather than the absolute error.

$$\mathrm{MAPE} = \frac{1}{n}\sum_{i=1}^{n} \left|\frac{\hat{y}_i - y_i}{y_i}\right| \times 100\% \tag{2.8}$$

2.3.1.1 Types of Neural Networks

Neural Networks come in various forms, each designed to suit specific applications and use cases. The following is a selection of different neural network types available for diverse tasks and use cases. There are 6 most commonly used types of neural networks, they are:

- Perceptron
- Feed Forward Neural Network
- Artificial Neural Network
- Convolutional Neural Network
- Recurrent Neural Network
- Long Short-Term Memory Neural Network

The table below, gives a description and the use case of the various types of neural networks.

Table 2.1: Summary of Neural Network Types, Descriptions, and Use Cases

Neural Network Type	Description	Use Cases
Perceptron	Simplest neural network; single-layer binary classifier.	Basic classification, linearly separable problems.
Feed Forward Neural Network (FFNN)	Neural network where data flows in one direction, from input to output.	Image classification, pattern recognition.
Artificial Neural Network (ANN)	General term for multi-layer neural networks inspired by the human brain.	Speech recognition, image classification, various tasks.
Convolutional Neural Network (CNN)	Network designed for grid-like data (e.g., images), capturing spatial features.	Image/video recognition, object detection.
Recurrent Neural Network (RNN)	Network with cycles, used for processing sequential data or time series.	Time-series forecasting, language modeling.
Long Short-Term Memory (LSTM)	A type of RNN designed to remember long-term dependencies in sequences.	Machine translation, speech recognition, time-series analysis.

3

Methodology

The objective of this thesis, is to measure pressure in a non-invasive approach and to use the pressure or strain readings as an input parameter to predict/estimate the SoH of the battery. In order to achieve this, the study was divided into 3 broad topics:

- Cell Modelling and Simulation
- Cell Level Testing (Dummy Cell and Active Cell)
- Deep Neural Network for State Estimation

The simulation and the dummy cell level testing were done to identify the optimal location on the cell to capture the changes in gas pressure inside the cell. Active cell testing was done to capture the real gas generation in a functional cell under a cyclic profile. The data gathered from the active cell level testing was then used for the state estimation using deep neural networks.

3.1 Modelling and Simulation : Can and Vent burst Li-ion cell

A 2-fold approach has been chosen to indirectly measure the pressure. Simulations and Dummy cell level testing is required to validate and arrive at a proof of concept to show that indirect pressure measurement is possible in a non-invasive approach. Different points in the cell were under consideration for indirect pressure measurement in the cell. As seen in Figure 3.1, various regions of the cell can be selected for monitoring or measuring the gas pressure inside the cell. The lid, large side of the cell can and the short side of the cell can are potential regions. In real-world applications, a single battery cell is not used as a stand-alone energy source, but batteries are connected in a particular parallel - series combination based on the use-case requirement to form the battery pack. These battery packs are then used in EVs and ESS. When batteries are placed in a battery pack, their large and short sides of the cell can become inaccessible due to the arrangement of batteries in a pack, the swelling force pads and the cooling systems to name a few. With the above constraints in a battery pack, the only region of the battery cell accessible for gas pressure measurement is the lid of the battery. The battery lid is the free surface of the cell (or even the battery pack), available to monitor to measure/capture the internal gas pressure of the cell. With the aim of determining optimal regions of the lid for gas pressure measurement, a simulation was performed to understand the behaviour of the lid to a ramp-up or a change in the gas pressure inside the cell body.

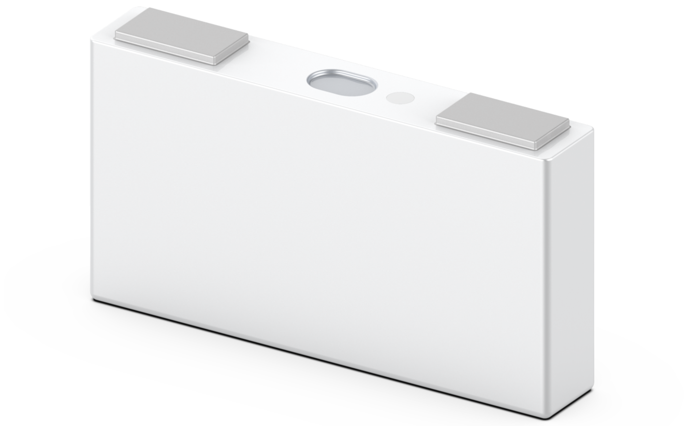

Figure 3.1: Prismatic Cell (orthogonal view)

After weighing all options mentioned in the previous section, strain gauges were chosen for the indirect pressure measurement. For determining the optimal locations or position in the cell lid for pressure measurement, a simulation study was done to simulate a vent burst and can burst scenario, where the cell can, cell lid and vent undergo deformation on ramping up the pressure. The simulation results would then give us optimal points of interest on the cell where we could mount the strain gauges and measure the pressure. This simulation was done to assess various regions of the cell lid for pressure measurement in a more visual approach to understand the behaviour of the cell lid and map out regions in the cell lid, cell-can weld interface and the vent of the cell and their corresponding behaviour to the varying pressure. The magnitude of the deformation or stresses developed in the process were not the focus of this simulation (as the dimensions of the cell (like cross-sectional thickness of the cell body or cell lid) used in this simulation is different from the dimensions of the cell in reality.

For the simulation study, the boundary conditions and the loading conditions were as shown in the Figure 3.7. All sides of the cell were constrained in all degrees of freedom with the Encastre boundary condition. The lid of the cell was allowed to be a free surface that could deform freely. The reason behind opting for the above mentioned boundary conditions was to replicate the real-life scenario where batteries are stacked or arranged in a particular manner in the battery pack (be it for EVs or ESS) with swelling force pads inserted between the cells (which help better thermal and mechanical damping). The pressure ramp up in the cell was simulated by ramping up the gas pressure inside the cell in all the directions of the cell volume with the same increase in the magnitude of the pressure as shown in Figure 3.6 and Figure 3.7 by the arrows. The pressure ramp-up used in the simulation was a quasi-static loading condition. Dynamic ram-up of pressure was not considered. The reason for this kind of load selection is due to the nature in which gas generation happens inside the cell, as a result of the chemical reactions and battery use-case. In reality the gas pressure ramp-up is in the order of 10^{-5} to 10^{-4} bar $\cdot$ s^{-1}. Since this rate of change of pressure in the active cell is very slow, we considered change in gas pressure per cycle (charging-rest-discharge-rest) to be quasi-static in nature. Figure 3.2 provides a visual understanding of the stress developed in the cell on increasing the gas pressure. We can see from Figure 3.2, that stresses are developed in the immediate region surrounding the vent area and also the lid-can weld seam. Stresses are also developed in and around the filling hole region near one of the cell terminals. The stresses indicated in Figure 3.2, is the vonMises stress and is indicated in MPa.

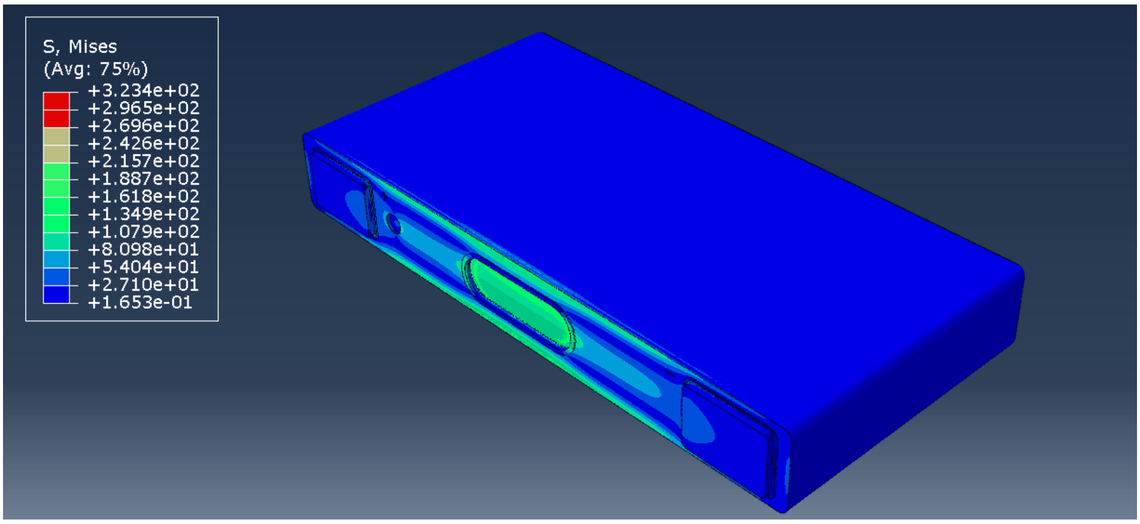

Figure 3.2: vonMises Stress developed in the cell

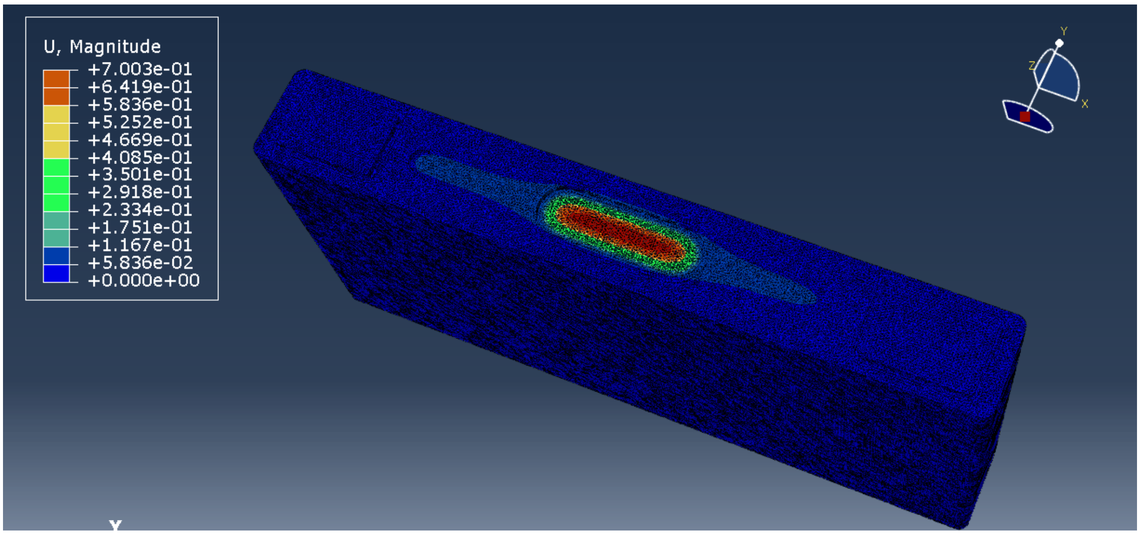

Figure 3.3: Deformation seen in the cell lid

The effect of pressure ramp-up, results deformation in the lids region can also be seen in Figure 3.3. The deformation in more prominent in the vent area and around the immediate surroundings of the vent. The magnitude of the deformation gradually fades as we move away from the lid towards the cell terminals. The deformation indicated in Figure 3.3, is in terms of mm. From the above results, we learn that, given the above mentioned boundary conditions and specified loading condition that mimicks the actual condition of the cell in the battery pack of an EV or ESS, 4 potential regions on the cell lid can be considered for capturing the change in gas pressure inside the cell. the regions of the lid under consideration are:

- Vent
- Region next to the vent, in the direction perpendicular to the lid width
- Region next to the vent, in the direction along the length of the lid
- Filling Hole

With the following observations, we then perform dummy cell level testing, to validate the proposed regions on the cell lid for pressure measurement.

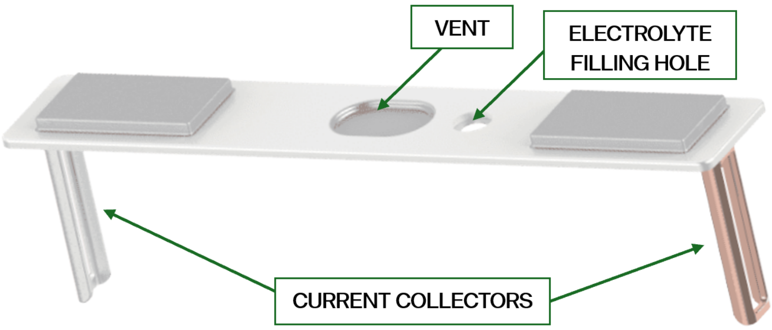

Figure 3.4: Cell Lid - Orthogonal view

Figure 3.4, is a component level view of the cell lid. The vent, and electrolyte filling hole are clearly indicated in the figure along with the current collectors.

3.2 Experimental Cell Testing

3.2.1 Dummy Cell Level Testing

A dummy cell is a fully assembled cell with jelly roll but does not contain the electrolyte. A dummy cell with jelly roll was chosen for the measurement study, in order to create a closest match to a real world scenario, that is to attain the closest possible match to the packing ratio seen in active cells. The packing ratio in cells (prismatic or cylindrical) can be visually studied with the help of a CT scan as shown in Figure 4.9. The constraints applied on the cell were done in order to mimick the real world scenario of batteries stacked in a battery pack. Since the aim is to mimick the real life battery usage in battery packs of EVs and ESS, the DuT is completely constrained in all directions with the help of rigid jigs and is clamped using U-clamps to enhance the rigidity of the jig, to restrict the deformation of the large and short sides of the cell body on increasing the gas pressure inside the control volume of the cell.

Figure 3.5: Exploded view of the Dummy Cell - lid and jelly roll (orthogonal view)

To ensure the cell is completely constrained in order to mimick the battery pack condition, the dummy cell as shown in Figure 3.5 is placed in jigs as shown in Figure 3.6 and Figure 3.7. A hole of 2mm diameter is made on the short side of the cell can. This hole is the inlet for the air into the dummy cell. Figure 3.6 & Figure 3.7, show us how the gas spreads and applies a uniformly distributed pressure inside the walls of the cell and on the cell lid. This is the pressure we are interested in capturing using strain gauges. As stated in Section 3.1, the pressure ramp-up or change in pressure inside the cell is quasi-static in nature. With this as reference, the pressure in the dummy cell during the test was a cyclical pressure load, where the gas pressure was increased from a minimum 0 bar to a specific maximum pressure. This pressure profile can be seen in Figure 3.8. Figure 3.8 shows the normalized pressure profile which is used to ramp up the pressure in the dummy cell,

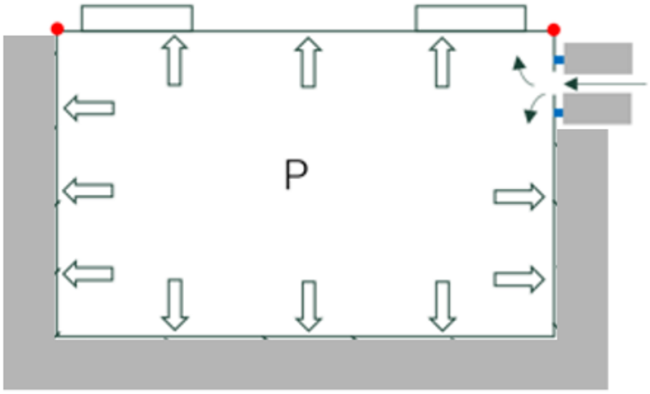

Figure 3.6: Front View of VBT

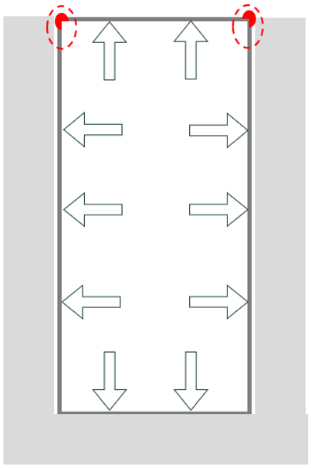

Figure 3.7: Side View of VBT

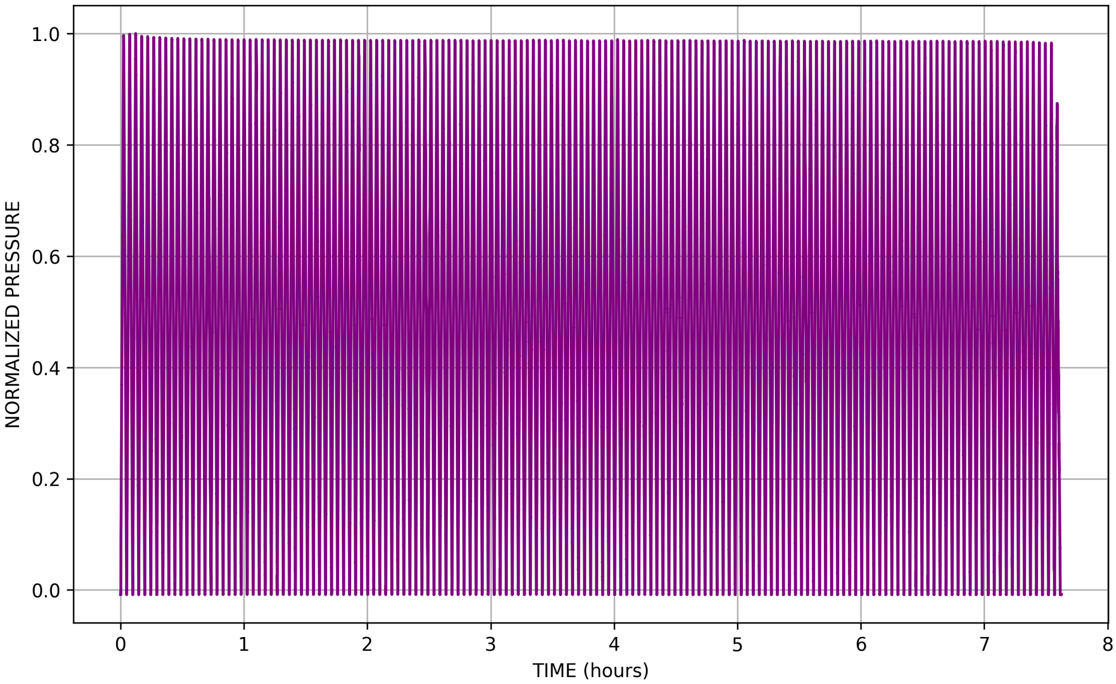

Figure 3.8: Plot of Normalized Pressure v/s Time

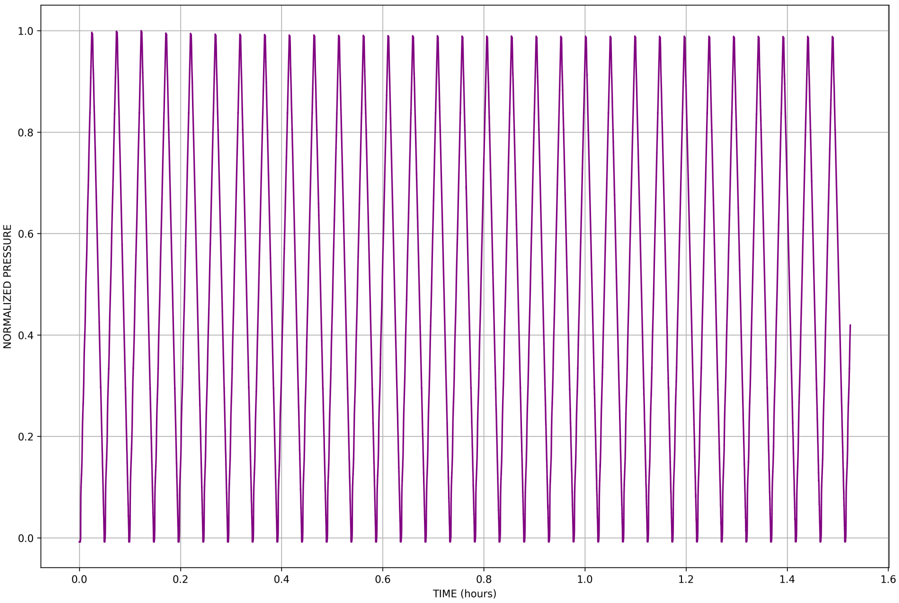

Figure 3.9: Plot of Normalized Pressure v/s Time (First 50 Cycles)

hold the pressure at the peak pressure for 5 seconds and ramp down the pressure back to 0 bar. This continuous ramp-up and ramp-down in gas pressure inside the cell was done for 150 cycles as shown in Figure 3.8. It must be noted that, in these tests, the rate of pressure ramp-up and pressure ramp-down is the same. The pressure ramp-up is done by an air pump that feeds air into the VBT based on the provided pressure ramp-up rate.

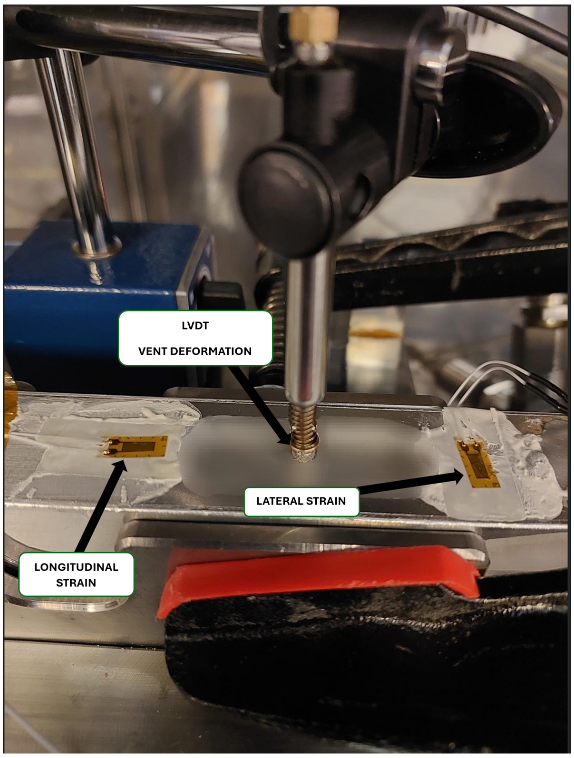

Figure 3.10: Dummy Cell VBT Setup

In Section 3.1, 4 different regions on the cell lid, suitable for pressure measurement was listed. Using this information, strain gauges were placed immediately next to the vent of the cell. Figure 3.9 shows the dummy cell with strain gauges attached to the lid. Two strain gauges have been used to capture both the lateral strain (strain measured in the direction perpendicular to the length of the lid) and longitudinal strain (strain measured along the length of the lid). Figure 3.10 also shows the LVDT being used to measure the deformation of the vent to corresponding changes in gas pressure inside the dummy cell. The normalized pressure profile as shown in Figure 3.8, which is facilitates, continuous ramp-up and ramp-down in gas pressure inside the cell is captured by the strain gauges and LVDT.

The corresponding lateral strain (μm/m), longitudinal strain(μm/m) and deformation of the lid (mm) is recorded. Since all the data and graphs presented in this report are normalized, the lateral strain, longitudinal strain and deformations measured by the LVDT are dimensionless.

3.2.1.1 Correlation Coefficient Matrix

The Pearson correlation coefficient, often denoted as r, is a statistical measure that quantifies the strength and direction of a linear relationship between two continuous variables. The correlation matrix calculates the correlation coefficients between pairs of variables. Specifically, it measures the degree to which two variables are linearly related. The correlation coefficient, often denoted as r, can range from -1 to $+1$, where $+1$ indicates a perfect positive linear relationship, -1 indicates a perfect negative linear relationship & 0 indicates no linear relationship. The relationship between lateral strain, longitudinal strain, the vent deformation and deformation of the electrolyte filling hole is analysed using the correlation coefficient matrix. The Pearson correlation coefficient is used to determine or calculate the linear relationship between continuously varying gas pressure and the corresponding respective lateral strain, longitudinal strain and vent deformation.

The Pearson correlation coefficient between two variables X and Y is given by:

$$r_{xy} = \frac{\mathrm{cov}(X, Y)}{\sigma_X \sigma_Y} \tag{3.1}$$

where:

- $\mathrm{cov}(X, Y)$ is the covariance of the variables X and Y,
- σ_X is the standard deviation of X,
- σ_Y is the standard deviation of Y.

3.2.2 Active Cell Cycling : Pressure Measurement

With the aim of measuring gas pressure generated inside the cell as a result of the chemical reactions that take place during the charge-discharge cycling of the cell, a harsh cycling profile was chosen, in-order to generate the maximum amount of gas inside the cell within the stipulated short duration available for testing, at our disposal.Perform cycling of active cells under pre-determined cycling conditions. Cycling conditions under consideration is 1C1C T45 cycling between 0% - 100% SoC. Strain Gauges will be used to measure the pressure within the cell in a non-invasive in-operando method.

3.2.2.1 Cycling Profile

The cycling profile chosen can be seen below in Figure 3.11.

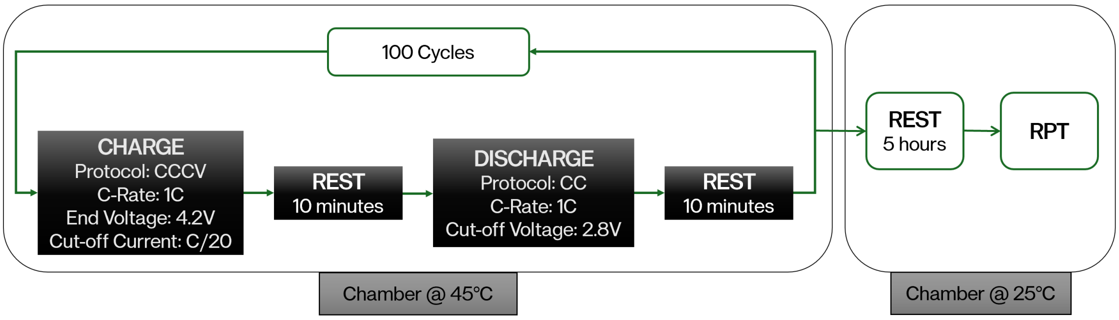

Figure 3.11: Cycling Profile for Active Cell

1 charging - discharging cycle is divided into 4 steps. The cell cycling begins at an elevated chamber temperature of 45 °C with charging at a C-rate of 1C. The CCCV protocol is employed for completely charging the cell. The cell is then allowed to rest for 10 minutes in order to reach an equilibrium state. The cell is then discharged at a C-rate of 1C down to a cut-off voltage of 2.8V. The cell is then allowed to rest

for a period of 10 minutes and the cycle repeats with charging. Once 100 cycles are completed, the chamber temperature is lowered to 25 °C. It is at 25 °C, that the RPT is done to calculate the DCIR and other parameters which are integral in assessing the capacity and health of the battery. The two shortened rest intervals of 10 minutes each, accelerate the aging of the cell and aid in harsher gas generation. The current and voltage profiles shown in Figure 3.12 - Figure 3.19 are for 100 cycles. This 100 cycles profile is repeated after RPT is done.

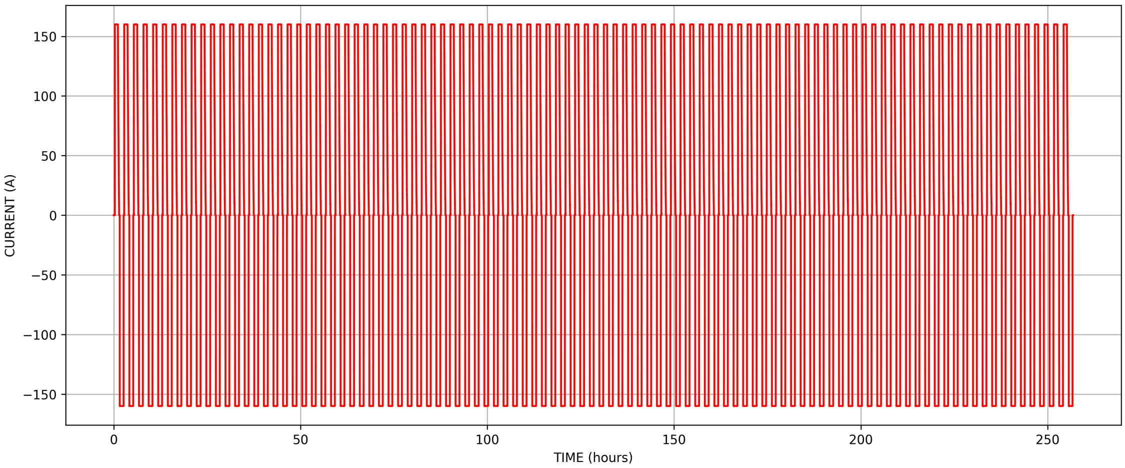

Figure 3.12: Cycling Profile : Current v/s Time

Figure 3.13 is a plot showing the extracted current profile of the first 5 cycles from the current profile shown in Figure 3.12.

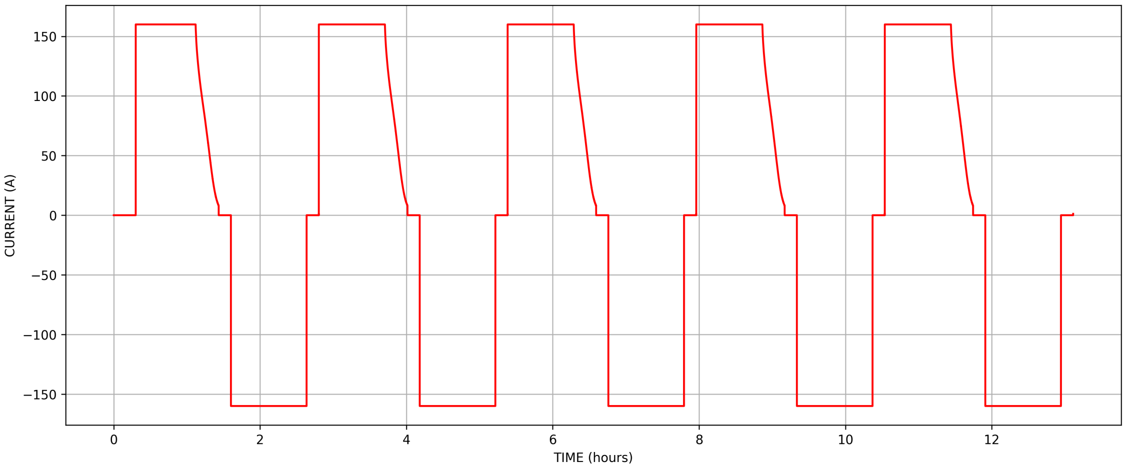

Figure 3.13: Cycling Profile : Current v/s Time (First 5 Cycles)

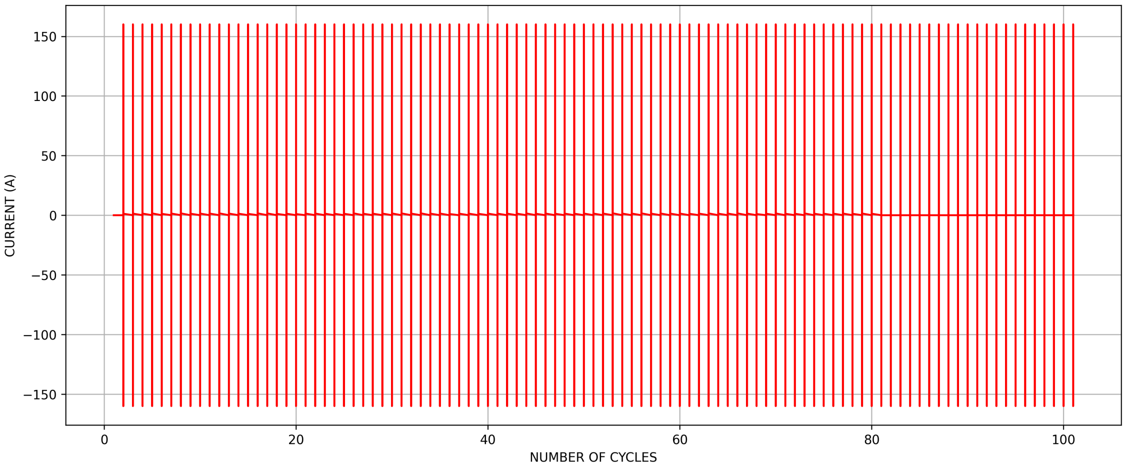

Figure 3.14: Cycling Profile : Current v/s Number of Cycles

Figure 3.15 is a plot showing the extracted current profile of the first 5 cycles from the current profile shown in Figure 3.14.

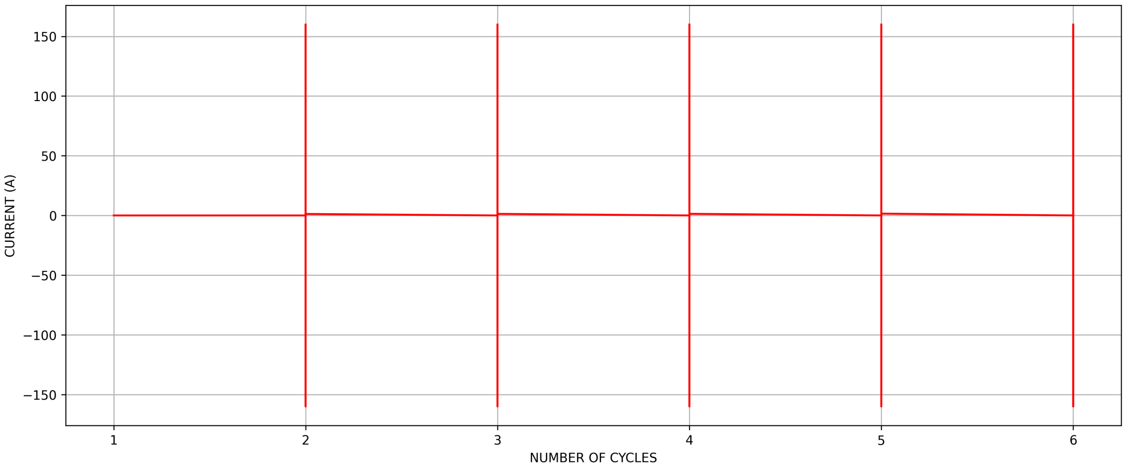

Figure 3.15: Cycling Profile : Current v/s Number of Cycles (First 5 Cycles)

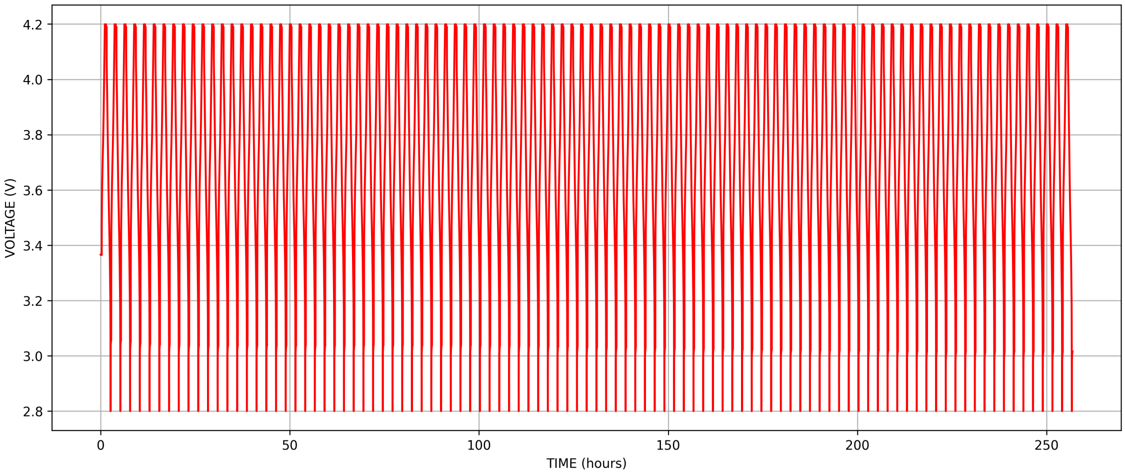

Figure 3.16: Cycling Profile : Voltage v/s Time

Figure 3.17 is a plot showing the extracted current profile of the first 5 cycles from the current profile shown in Figure 3.16.

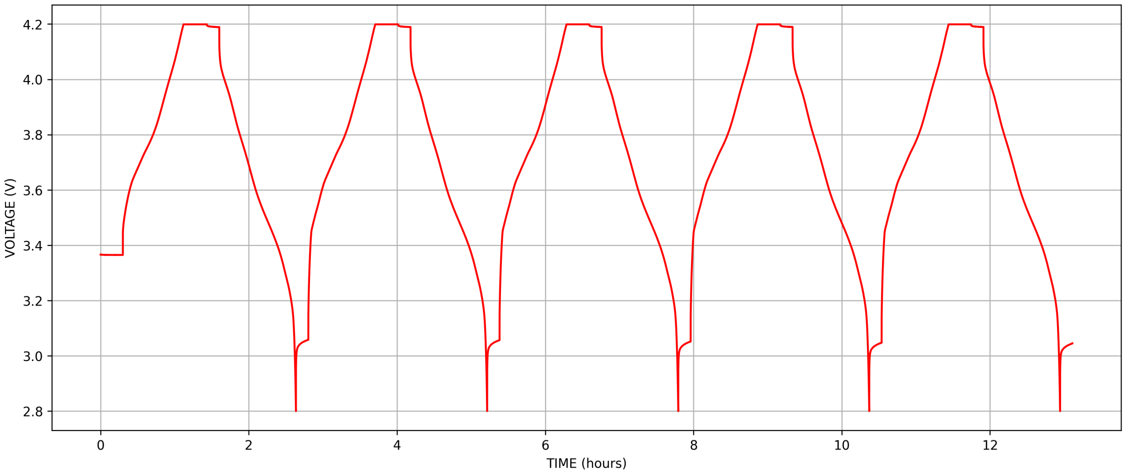

Figure 3.17: Cycling Profile : Voltage v/s Time (First 5 Cycles)

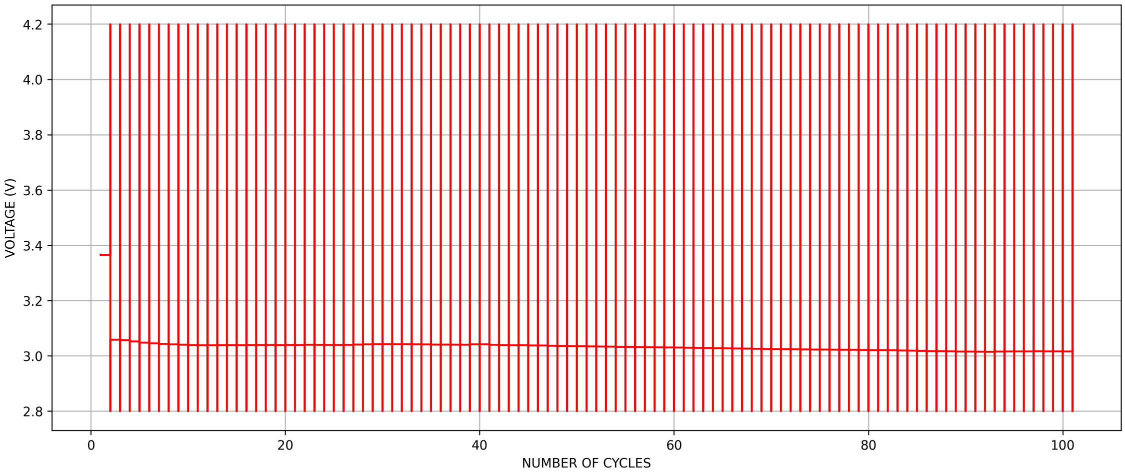

Figure 3.18: Cycling Profile : Voltage v/s Number of Cycles

Figure 3.19 is a plot showing the extracted current profile of the first 5 cycles from the current profile shown in Figure 3.18.

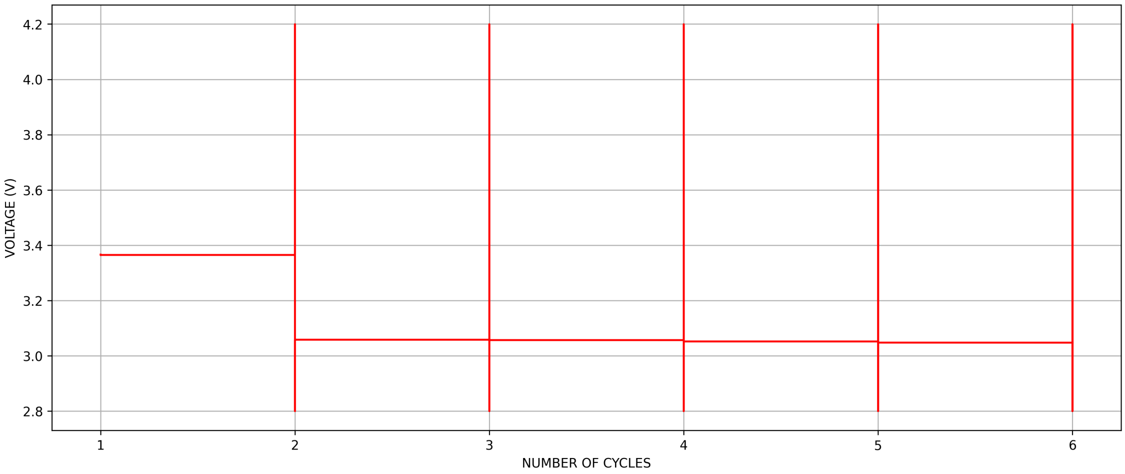

Figure 3.19: Cycling Profile : Voltage v/s Number of Cycles (First 5 Cycles)

3.3 State Estimation using Deep Neural Networks

3.3.1 Strain-Pressure Neural Network Model

In order to estimate/predict the gas pressure generated inside the cell, using strain readings from strain gauges attached to the lid of the cell, we developed a deep neural network (DNN) model to predict pressure from a set of time-series data including time, lateral strain, strain rate, and temperature. The process began with loading and concatenating data from multiple sheets in Excel files, followed by interpolating the datasets to ensure uniform length. After combining these inputs, split the data into training and test sets and standardized the inputs. A sequential DNN model was developed, with multiple layers and dropout for regularization, and trained it using the Stochastic Gradient Descent (SGD) optimizer with a learning rate scheduler. The model's performance was evaluated using Mean Squared Error (MSE) on the test set using (2.7), and predictions were made on new data. The DNN developed had 1 input layer with 4 input parameters (time, strain, strain rate and cell temperature), 4 hidden/dense layers and an output layer with one uotput parameter (predicted pressure). Hyperparameters of the DNN are as shown in Table 3.1. The model was trained and tested against measured gas pressure values of similar cells and similar cycling profile.

Table 3.1: Hyperparameters of the Neural Network Strain-Pressure Estimation

Neural Network - Hyper Parameters	
Hyperparameter	**Settings**
Number of Hidden Layers	4
Number of Neurons in Hidden Layer	256 : 128 : 64 : 32
Learning Rate	0.0001
Neuron Initialization	He initialization
Optimization Algorithm	SGD
Activation Function	Linear
Loss Function	Mean Squared Error (MSE)
Dropouts	0.2
Batch Size	128
Batch Normalization	After non-linearity
Validation Split	0.2

3.3.2 Strain-Pressure-SoH Neural Network Model

In order to estimate/predict the gas pressure generated inside the cell, using strain readings from strain gauges attached to the lid of the cell, we developed a deep neural network (DNN) model to predict pressure from a set of time-series data including time, lateral strain, strain rate, and temperature. The process began with loading and concatenating data from multiple sheets in Excel files, followed by interpolating the datasets to ensure uniform length. After combining these inputs, split the data into training and test sets and standardized the inputs. A sequential DNN model was developed, with multiple layers and dropout for regularization, and trained it using the Stochastic Gradient Descent (SGD) optimizer with a learning rate scheduler. The model's performance was evaluated using Mean Squared Error (MSE) on the test set using (2.7), and predictions were made on new data.

The DNN developed had 1 input layer with 4 input parameters (time, strain, strain rate and cell temperature), 4 hidden/dense layers and an output layer with one uotput parameter (predicted pressure). Hyperparameters of the DNN are as shown in Table 3.2. The model was trained and tested against SoH values and other battery health indicators.

Table 3.2: Hyperparameters of the Neural Network for Strain-SoH Estimation

Neural Network - Hyper Parameters	
Hyperparameter	**Settings**
Number of Hidden Layers	4
Number of Neurons in Hidden Layer	256 : 128 : 64 : 32
Learning Rate	0.0001
Neuron Initialization	He initialization
Optimization Algorithm	SGD
Activation Function	ReLU (Hidden Layers) & Linear (Output Layer)
Loss Function	Mean Squared Error (MSE)
Dropouts	0.2
Batch Size	64
Batch Normalization	After non-linearity
Validation Split	0.2

4

Results

The results of the Dummy cell level testing, Active cell testing and the estimation of internal gas pressure and SoH of the battery with the help of deep neural network (DNN) model, are discussed in this section of the report. This section deals with results, discussions and analyses.

4.1 Preliminary Results

With the aim of estimating/predicting the internal gas pressure inside the battery cell (here Li-ion), 4 points on the cell lid were chosen as regions of interest, for capturing the cell(cell lid) behaviour to changing internal gas pressure, as discussed in Section 3.1. Measuring devices such as strain gauges and LVDT were chosen for capturing the lid behaviour at the aforementioned 4 regions of the lid as shown in Figure 3.10, to measure the deformation caused on the cell lid due to change in internal gas pressure.

4.1.1 Dummy Cell Strain-Pressure Measurements

This section presents the results obtained by performing the dummy cell level tests as mentioned in Section 3.2 of this report. The following are the plots and results of the measurements made by the strain gauges placed on the lid, measuring the strain (in the lateral & longitudinal direction with respect to the length of the lid) and the LVDT measuring the deformation of the vent and the electrolyte filling hole, to changing internal gas pressure. The strain gauge measuring strain in the lateral direction with respect to the lid (lateral strain), the strain gauge measuring strain in the longitudinal direction with respect to the lid (longitudinal strain), the LVDT measuring the deformation of the vent and the deformation of the electrolyte filling hole are shown in Figure 3.10.

Figure 4.1 & Figure 4.2 are plots depicting the lateral strain captured by the strain gauges to changing gas pressure. As shown in Figure 3.8, the dummy cell is cycled between a minimum pressure of 0 bar to a particular maximum pressure P_{max} and this is repeated for over 150 cycles. This cyclical nature of the pressure profile, is also reflected in the normalized lateral strain measurements as indicated in the plot shown in Figure 4.1 & Figure 4.2. It can be seen in Figure 4.1, that at the start of the test, the strain reading with respect to pressure initially drops and becomes negative. With a further pressure increase, from the minimum gas pressure of 0 bar, the strain readings, measured by the strain gauge, measuring the strain in the lateral direction, gets rectified and begins to increase as the pressure further increases to a particular maximum pressure $P_{\max}$.

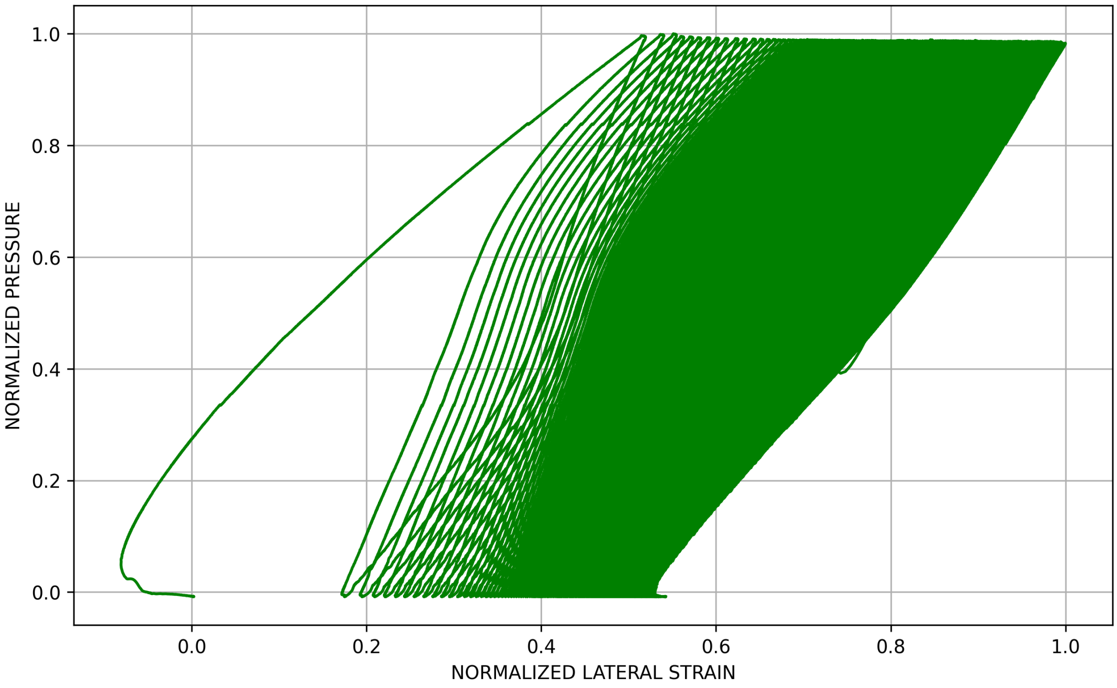

Figure 4.1: Plot of Normalized Pressure v/s Normalized Lateral Strain

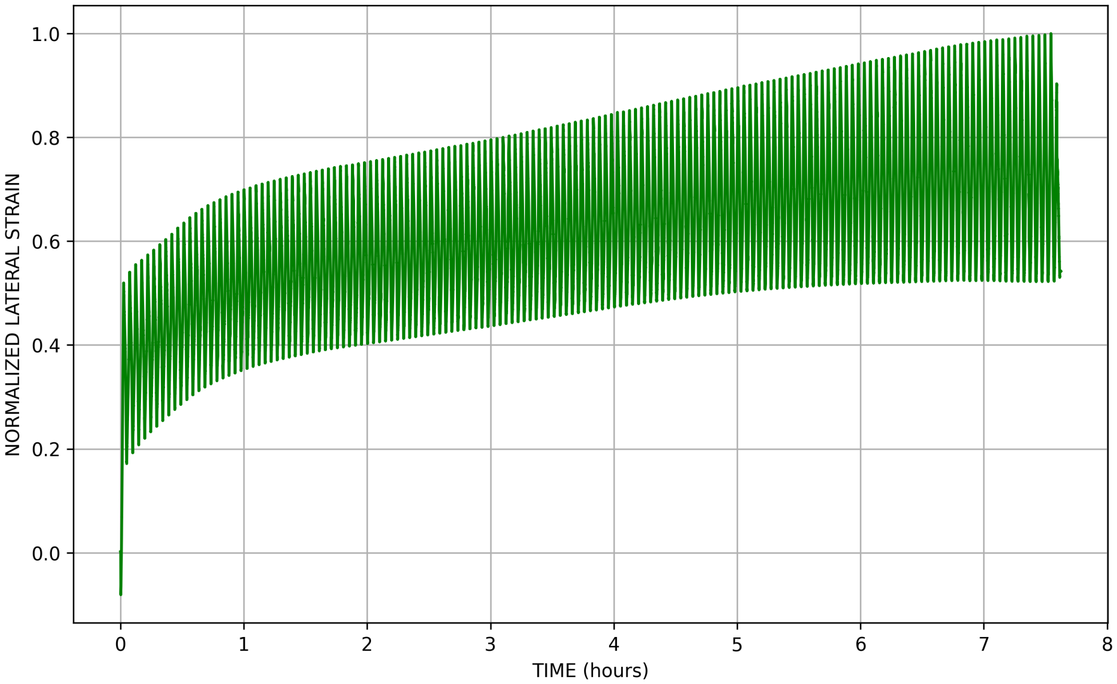

Figure 4.2: Plot of Normalized Lateral Strain v/s Time

A similar behaviour as seen in the normalized lateral strain gauges measurements, is noticed with the measurements captured by the strain gauges oriented in the longitudinal direction as seen in Figure 4.3 & Figure 4.4.

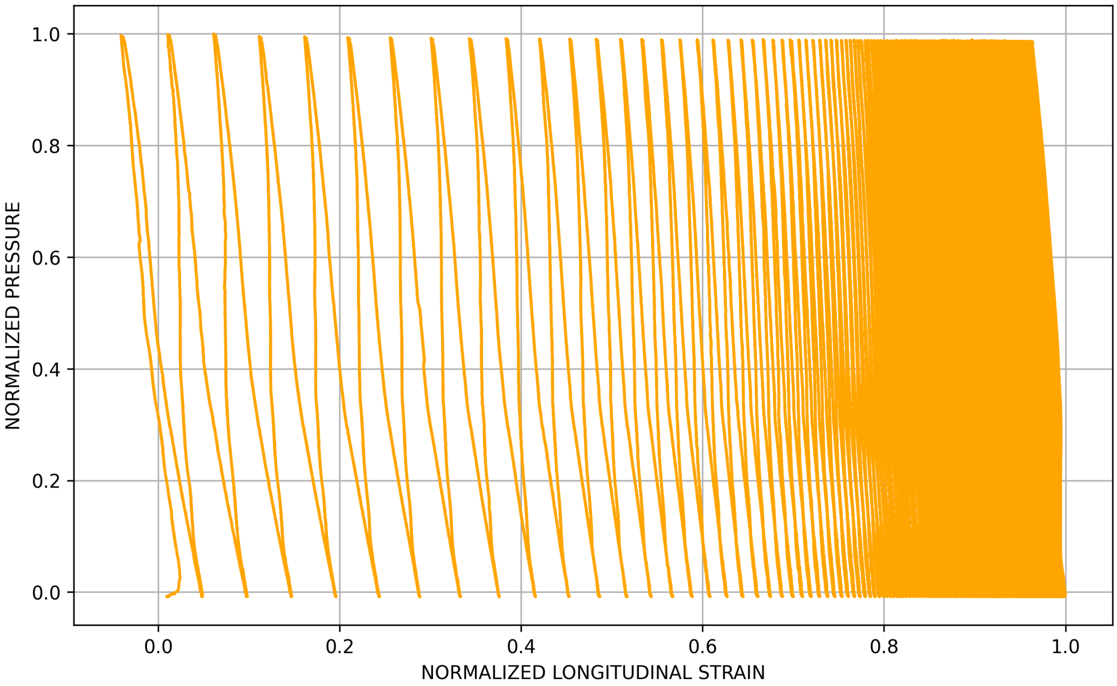

Figure 4.3: Plot of Normalized Pressure v/s Normalized Longitudinal Strain

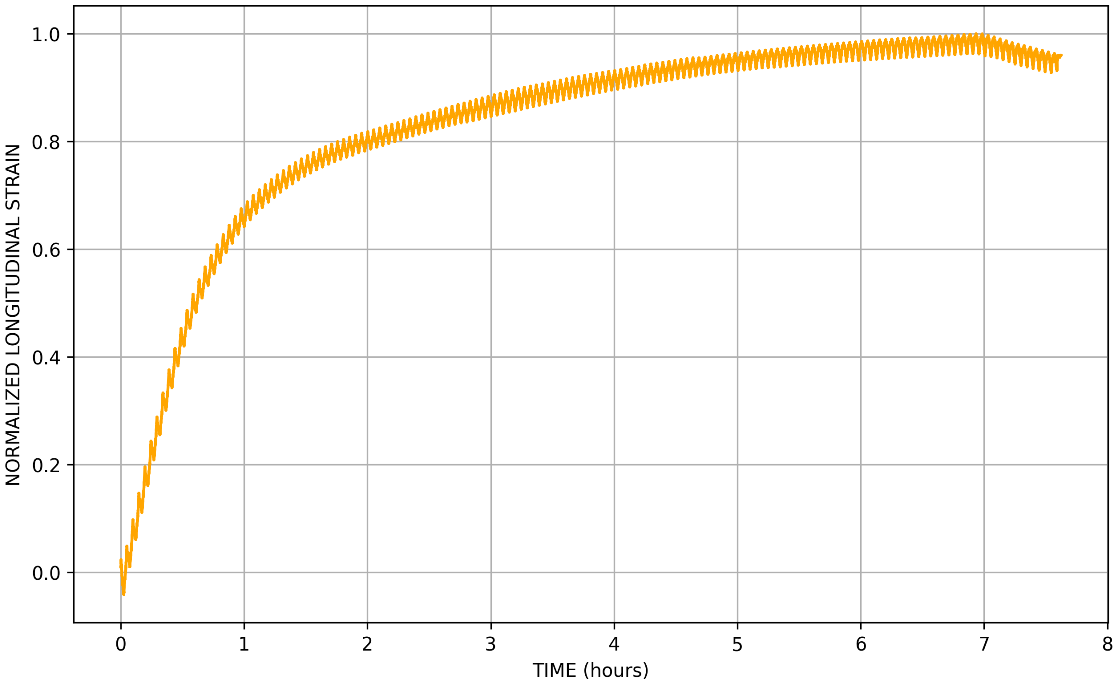

Figure 4.4: Plot of Normalized Longitudinal Strain v/s Time

Figure 4.5 is a plot depicting the deformation of the vent to changes in the supplied gas pressure. Figure 4.6 is a plot depicting the increase in the vent deformation with the passage of time as the number of cycles inches closer to 150 cycles.

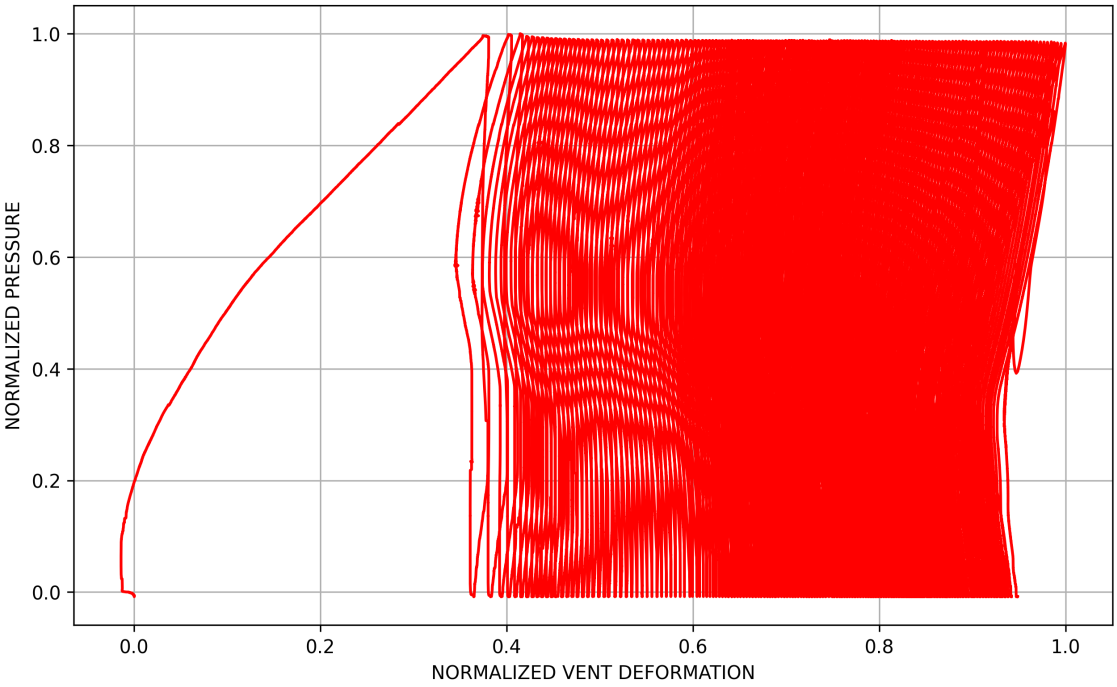

Figure 4.5: Plot of Normalized Pressure v/s Normalized Vent Deformation

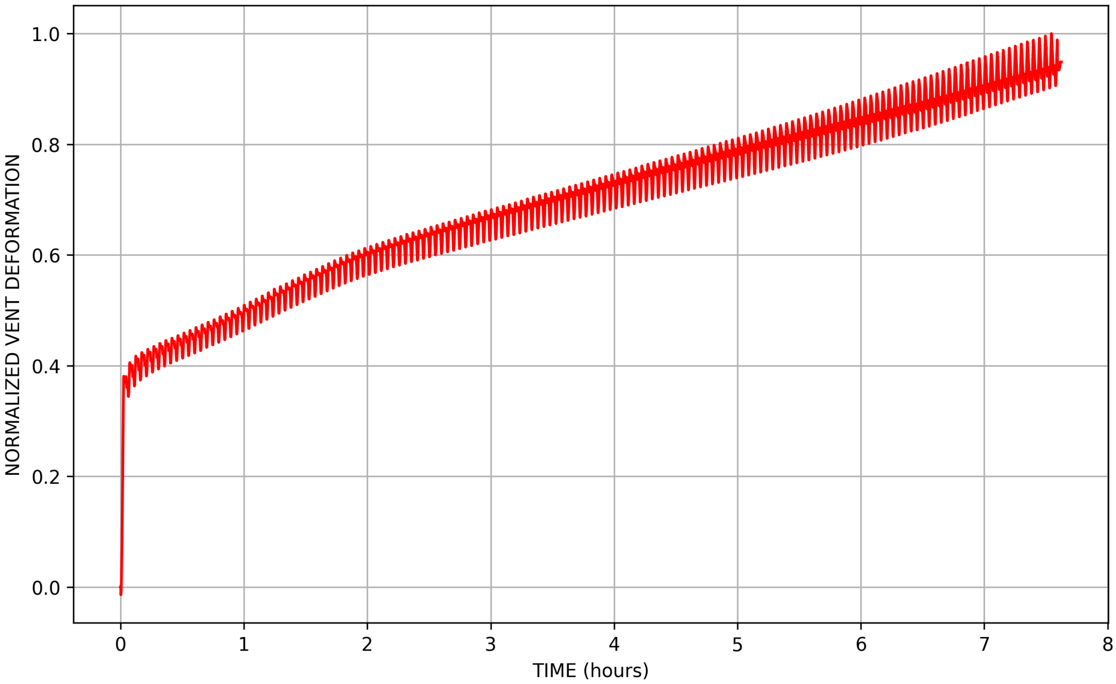

Figure 4.6: Plot of Normalized Vent Deformation v/s Time

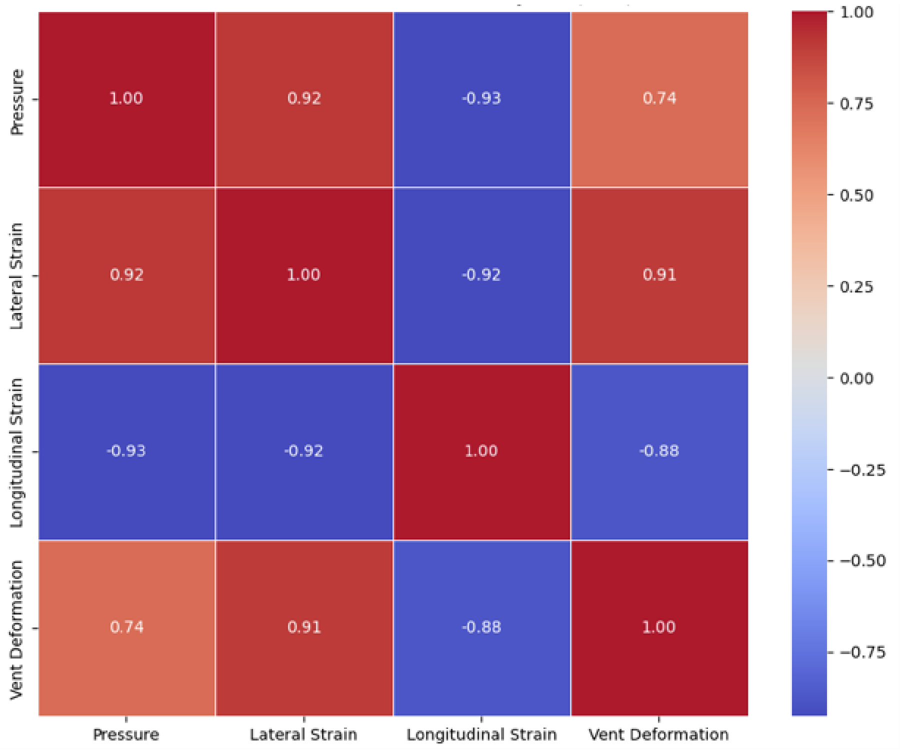

Figure 4.7: Correlation Coefficient Matrix - Vent Deformation

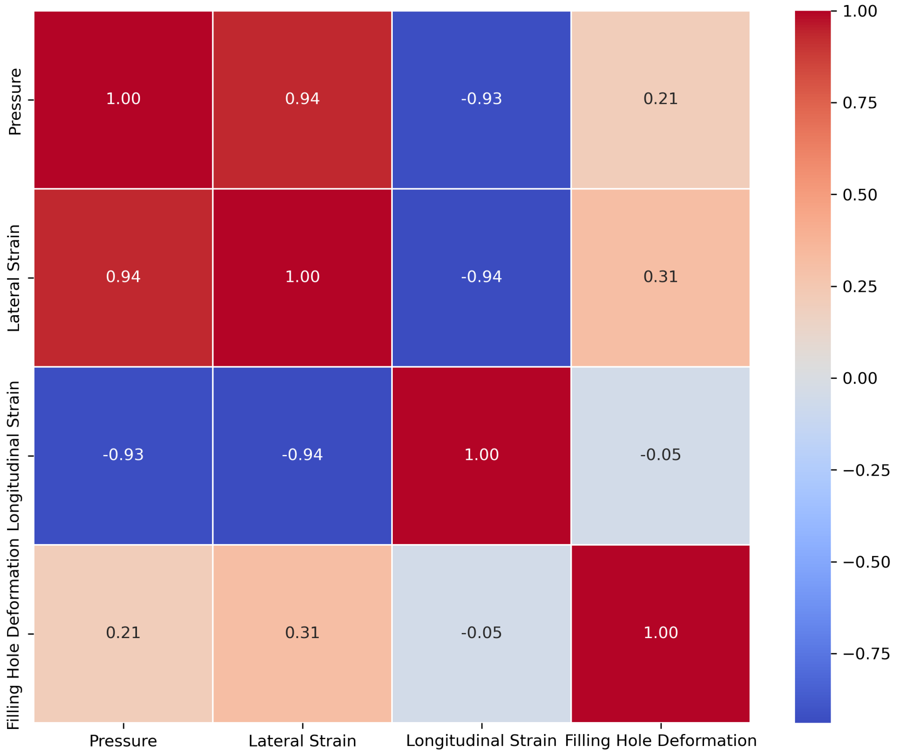

Figure 4.8: Correlation Coefficient Matrix - Electrolyte Filling Hole Deformation

The Correlation coefficient matrix shown in Figure 4.7, shows that Lateral strain has an almost direct positive linear relation ship with changing gas pressure. A

Pearson correlation of 0.92 exists between lateral strain and gas pressure, whereas longitudinal strain has a negative Pearson correlation of -0.93. The corresponding vent deformation has a positive Pearson correlation of 0.74, to respective changes in the supplied gas pressure. It can also be seen from Figure 4.8, that the electrolyte filling hole has a very poor Pearson correlation of 0.21 to changing supplied gas pressure. Other parts of the lid like the vent and the filling hole were not suitable for accurately capturing the changing gas pressure inside the cell.

Table 4.1: Pearson Correlation Coefficient of the 4 selected points on Lid

Pearson Correlation Coefficient	
Point of Interest on Lid	**Pearson Correlation**
Pressure - Lateral Strain	0.92
Pressure - Longitudinal Strain	-0.93
Pressure - Vent Deformation	0.74
Pressure - Electrolyte Filling Hole	0.21

From Figure 4.2, Figure 4.4 and Figure 4.6, it can be seen that with increasing number of cycles, the regions surrounding the vent and the vent itself begin to retain some residual plastic deformations as seen in the pictures. It is this residual plastic deformation that helps us capture the behaviour of the lid and the vent over the cycle life of the cell. It can be referred from the above mentioned figures, that each of the measurements - the normalized lateral strain, normalized longitudinal strain and the normalized vent deformation respectively have varying amplitudes in the recorded data. These amplitudes indicated the sensitivity of the measuring element to changes in the specimen (here changes in gas pressure inside the dummy cell). This higher amplitude aids in a more accurate and precise data collection, which is then used an input parameter for state estimation. This is the reason, that though, the normalized lateral strain and normalized longitudinal strain values recorded as shown in Figure 4.2 & Figure 4.4, respectively have a good response to changing pressure over time, we opt for choosing lateral strain measurements for capturing the response of the lid to changing internal gas pressure. This can also be backed by the values displayed in Table 4.1.

Hence from Table 4.1, we can conclude that since the strain measures in the lateral direction of the lid/cell, has a positive pearson correlation with internal gas pressure and lateral strain, (in this case normalized lateral strain) if is best suited to indirectly measure the gas pressure inside the cell. The vent deformation and deformation of the electrolyte filling hole can be neglected as they do not have a very good linear relationship to pressure. Longitudinal strain can be used, as it has a negative linear correlation with pressure, but to simplify and obtain better repeatability of measurements, it is advisable to neglect the longitudinal strain measurements for this study. The slight deviation of 0.08 $(1 - 0.92)$ in the Pearson correlation can be attributed to the packing ratio of the jelly roll in the cell can body, as seen in Figure 4.9. The CT scan shows us the empty gaps and certain irregularity that could be the cause for the slight deviation of the Pearson correlation of lateral strain (normalized lateral strain) with respect to Pressure from 1.

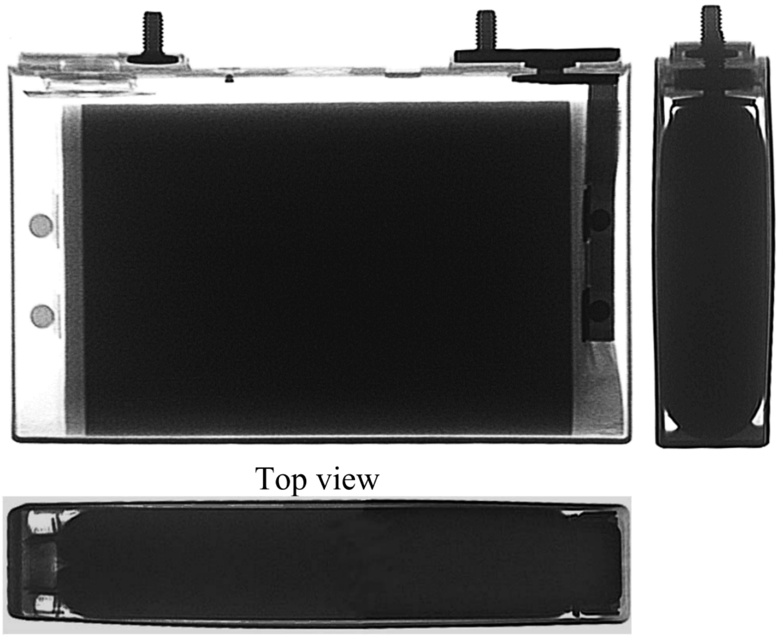

Figure 4.9: CT Scan of a Prismatic Cell

4.2 Active Cell Strain Measurements

Active Cell testing was done on 4 prismatic cells. All 4 prismatic cells have the same chemical composition, and physical dimensions. All 4 prismatic cells were cycled using the same profile as shown in Figure 3.11. 3 prismatic cells were regular cells without the gas pressure sensor inserted to the cell and 1 prismatic cell with the modification on the lid to mount the gas pressure sensor. Strain gauges were mounted on the 3 regular cells (cells without modification for gas pressure sensor). Cell 1 and Cell 2 had only 1 strain gauge mounted just next to the vent area as shown in Figure 3.10 and this strain gauge measures the strain in the lateral direction with respect to the lid. The type of strain gauge used for Cell 1 and Cell 2 is shown in Figure 3.10, where there is only one measuring grid in the strain gauge and it measures the strain only in 1 direction (that is along the length of its grid). Cell 3 was mounted with a bi-directional strain gauge, which has two measuring grids, positioned perpendicular to each other as shown in Figure 2.13. A bi-directional strain gauge was used in Cell 3 to monitor both the lateral and longitudinal strain developed in the cell over the cycling profile. It must be noted that all the strain gauges were mounted on the same side of the vent, in order to get more accurate and comparable results.

All 4 cells underwent 500 Cycles for the profile shown in Figure 3.11. The reason for testing the cells upto 500 cycles, was to get a good amount of raw data that we could then use as input variables/parameters to train and test the DNN. Figures 4.9 to 4.11, present the lateral strain readings of the 3 cells having the same chemistry and cycled using the same profile after 500 Cycles of testing.

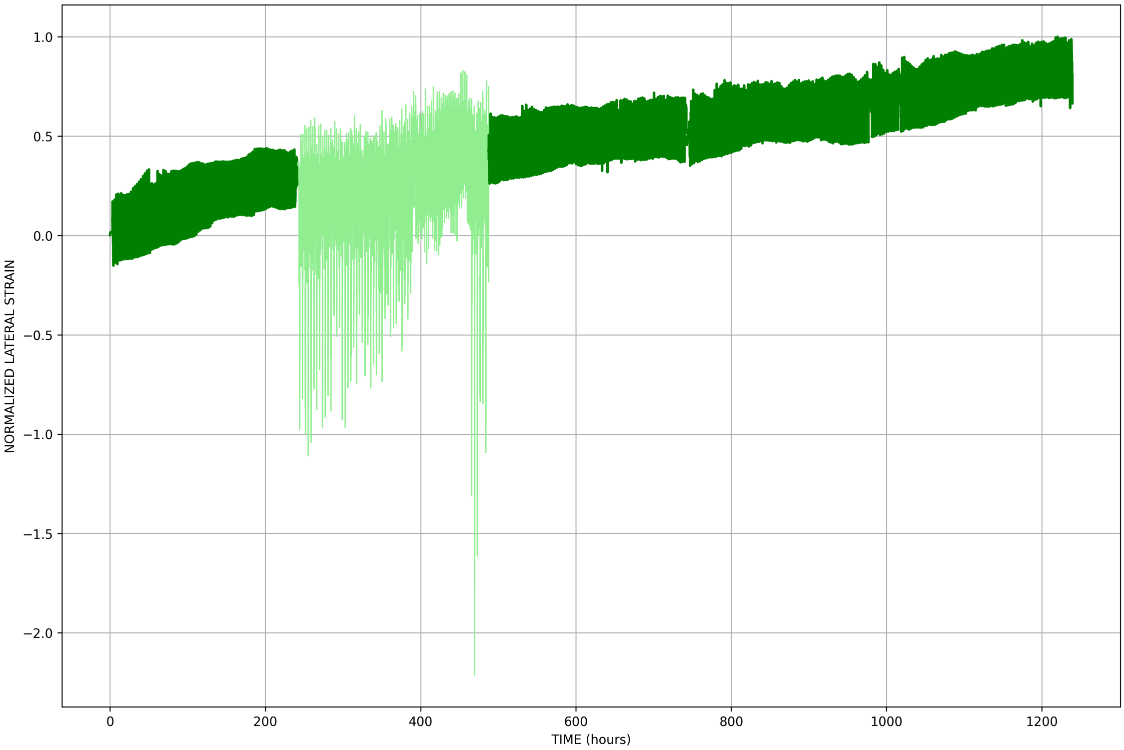

Figure 4.10: Plot of Normalized Lateral Strain v/s Time (0-500 Cycles) : Cell 1

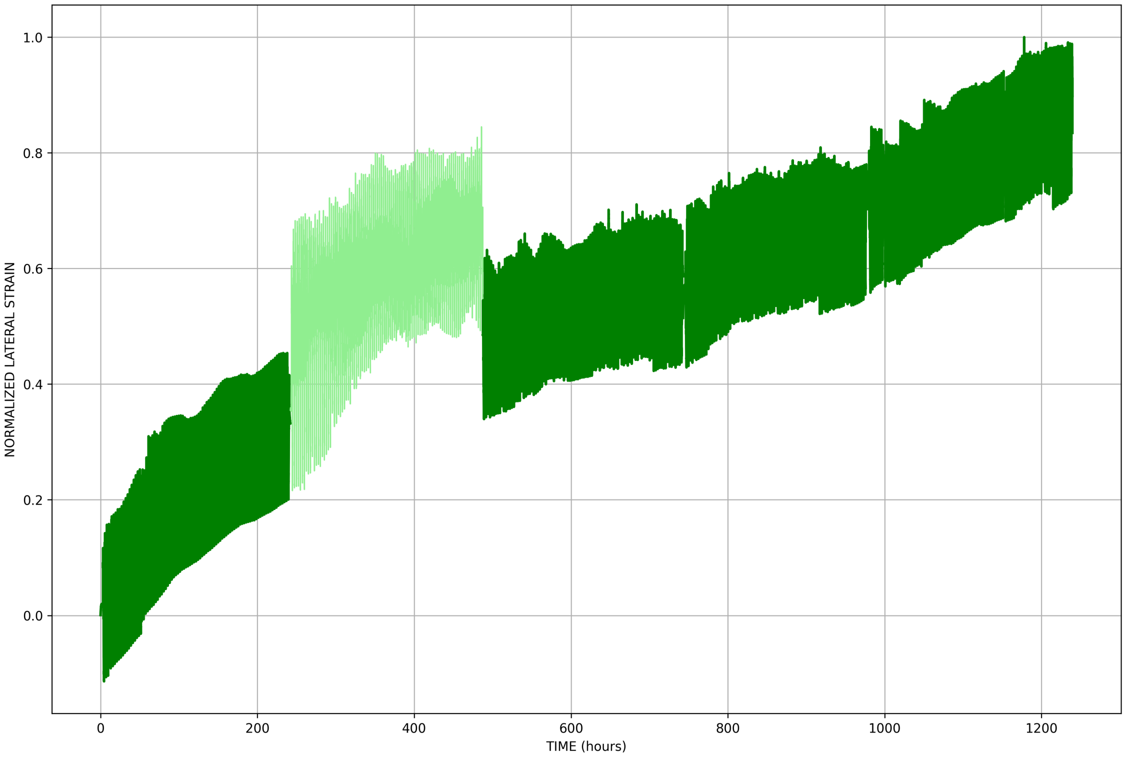

Figure 4.11: Plot of Normalized Lateral Strain v/s Time (0-500 Cycles) : Cell 2

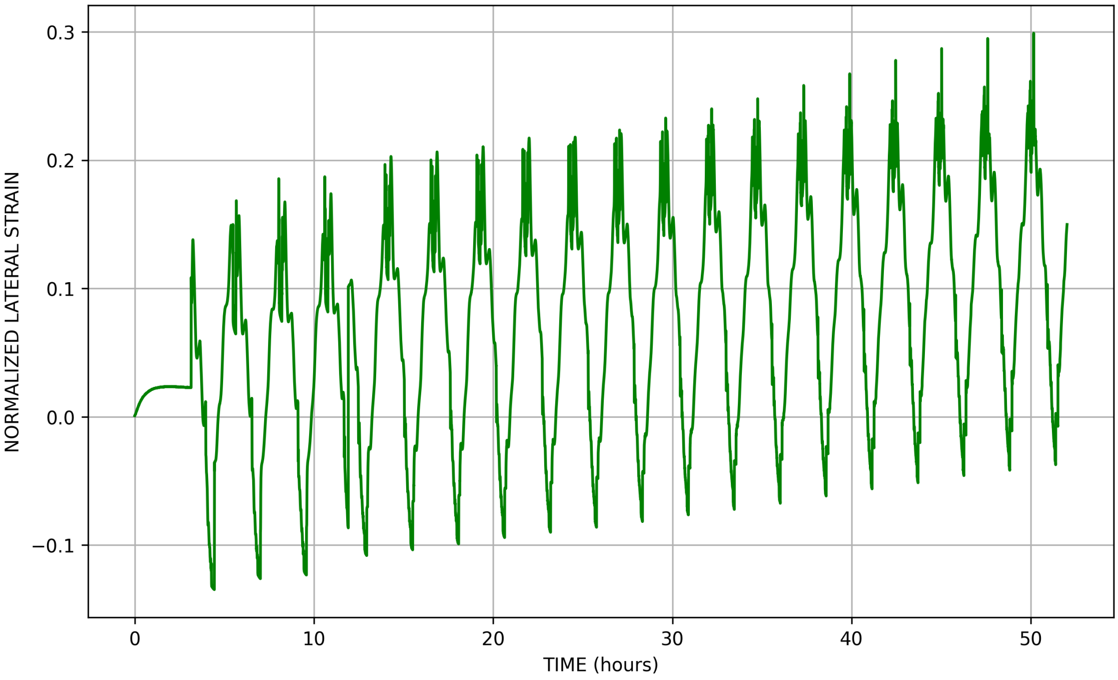

Figure 4.12: Plot of Normalized Lateral Strain v/s Time (First 20 Cycles) : Cell 2

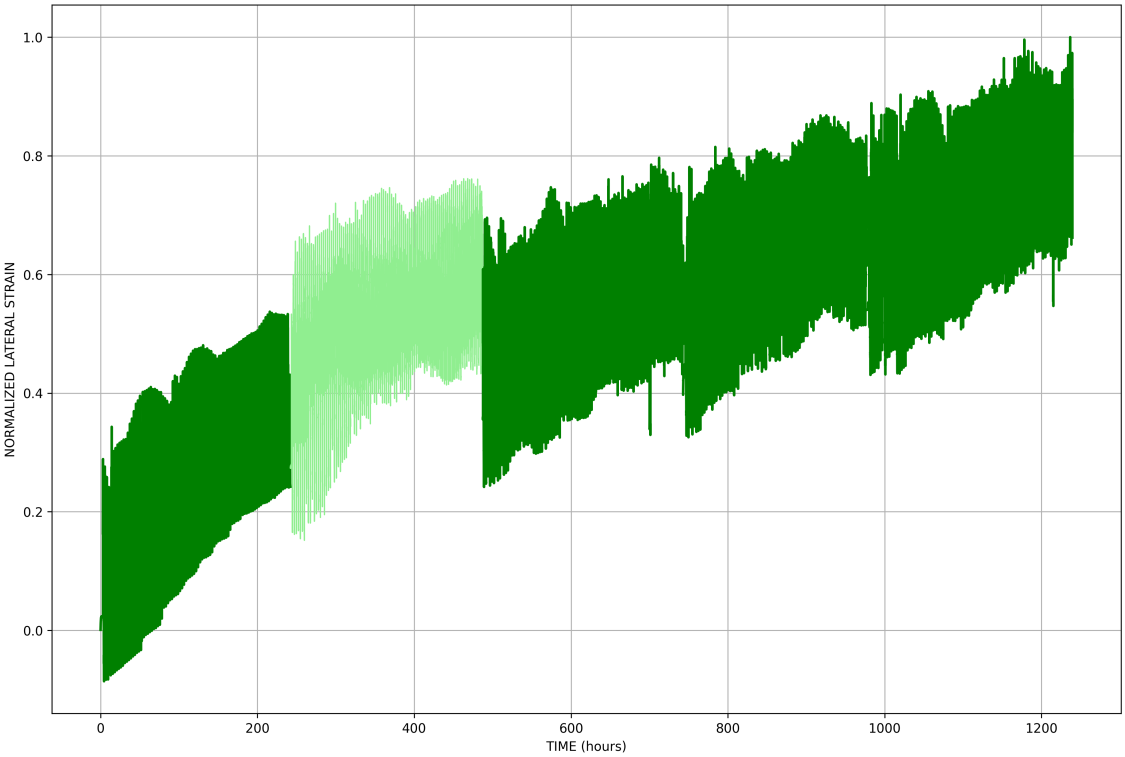

Figure 4.13: Plot of Normalized Lateral Strain v/s Time (0-500 Cycles) : Cell 3

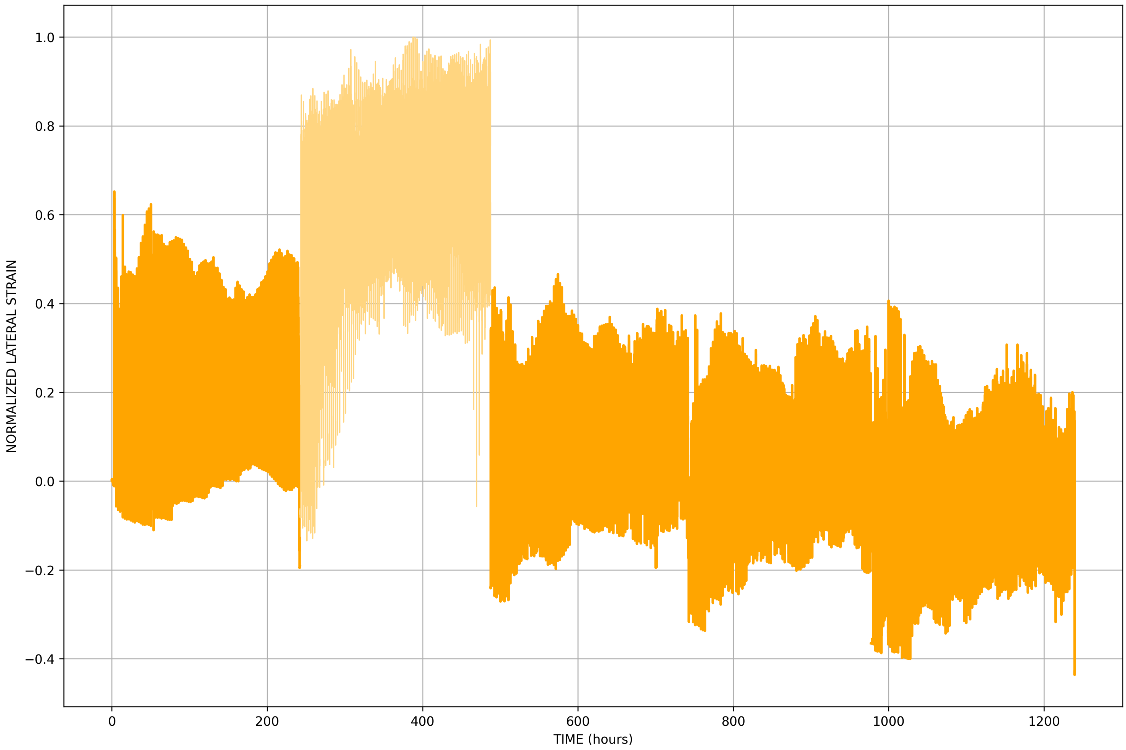

Figure 4.14: Plot of Normalized Longitudinal Strain v/s Time (0-500 Cycles) : Cell 3

Figure 4.12, is a zoomed in version of the Figure 4.11, in which the lateral strain measurements of only the first 20 cycles is shown for a better visual understanding of the trends in the strain readings. From the Figure 4.10, Figure 4.11, Figure 4.13 & Figure 4.14, we can see that the the readings are consistent and follow the expected trend, except for a small portion between 100 - 200 cycles. In this interval of cycling, dude to minor issues with the data logger, the measured strain has deviated to a small degree. This can be clearly seen in Normalized lateral strain readings in Cell 1 and Cell 2. The issue with the data logger was rectified and the strain readings of the consecutive cycles was not affected. The normalized longitudinal strain as shown in Figure 4.14, shows that, as the number of test cycles gradually increases, the longitudinal strain measured by the strain gauge gradually decreases and starts moving towards the negative domain of the strain readings. This normalized strain data can be used to train the DNN, for pressure estimation, but to avoid complexity the longitudinal strain data has not been used in the pressure estimation. With the aim of predicting the pressure using the strain data, the above strain data along with temperature and time were used to estimate/predict the internal gas pressure inside the active cell. It can be seen from the above results that lateral strain readings are more consistent and predictable as compared to the longitudinal strain readings. Hence, the lateral strain readings are used for the strain-pressure prediction using artificial neural network.

4.3 Active Cell Strain - Pressure Prediction

The cells were tested for 500 cycles. The strain data collected from the active cell testing can now be used as an input to the DNN models developed for estimating the internal gas pressure of the cell. To predict the pressure, 3 inputs were given to the DNN model to train and test the model. The initial 3 input parameters were time, strain and strain rate. This was fed to the model and the model was trained with this input data against the pressure data recorded using the gas pressure sensor. To this trained DNN model, new set of input data was fed to predict the gas pressure inside the cell. The following plot as shown in Figure 4.15 was obtained along with the training loss as shown in Figure 4.16. The plot shown in Figure 4.15 was obtained after feeding data obtained post the completion of 300 cycles of testing. For this trial of predicting the pressure, the Adam activation function was used with different learning rates and number of hidden layers. The predicted pressure using this model was not very accurate to the pressure data obtained from the gas pressure cells.

With the aim of better understanding the mechanical behaviour of the cell during cycling, we decided to also include the cell temperature as an additional input parameter to the DNN model for training, testing and prediction. In the new DNN model developed as described in Table 3.1, this time 4 input variables were fed to the DNN model for training the model, testing the model and for further predicting the gas pressure inside the cell.

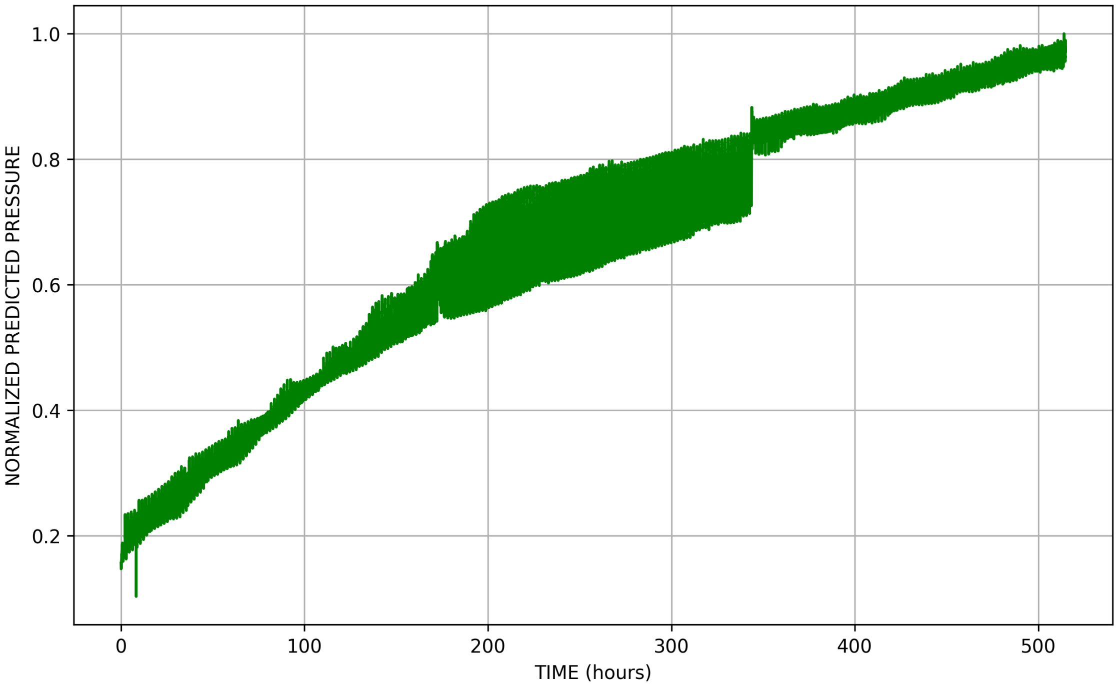

Figure 4.15: Plot of Normalized Predicted Pressure v/s Time of an Active Cell

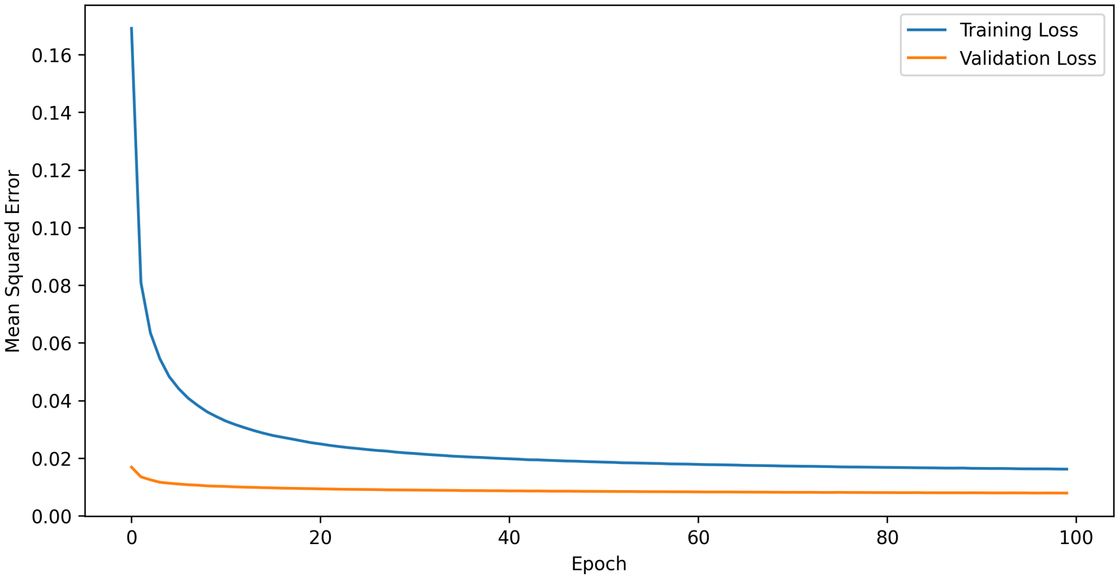

Figure 4.16: Plot of Training Loss and Validation Loss v/s Number of Epochs

With the aim of better understanding the mechanical behaviour of the cell during cycling, we decided to also include the cell temperature as an additional input parameter to the DNN model for training, testing and prediction. The cell temperature recorded in this case is the cell surface temperature around the vent area of the cell. The reason for including temperature, is that gas pressure is affected by the temperature of the cell, gas pressure slightly increases with increase in temperature. Hence to include this variation of gas pressure with temperature, the cell temperature was also considered as an input for the DNN. In the new DNN model developed as described in Table 3.1, this time 4 input variables were fed to the DNN model for training the model, testing the model and for further predicting the gas pressure inside the cell. The input parameters now were : Time, Stain (Lateral Strain), Strain Rate (obtained from lateral strain and time) and Cell Temperature. With these 4 input parameters and the gas pressure data obtained from the gas pressure sensor gathered after 500 cycles of testing, the DNN model was trained and tested. Then a new set of time, strain, strain rate and cell temperature data was provided to the DNN model for the gas pressure prediction. The Lateral strain data from Cell 2 and Cell 3 was used for the training, testing and prediction. The predicted gas pressure inside the cell, for Cell 2 and Cell3 are shown in Figure 4.17 and Figure 4.19 respectively. The training and validation loss for both Cell 2 and Cell 3 data after predicting the gas pressure using the DNN model is as shown in Figure 4.18 and Figure 4.20 respectively. From the training and validation loss plots, we can see that there is a smooth and close convergence of the training loss and the validation loss, depicting that the DNN model is not over fitting, the model has learnt the data patterns well and is able to predict as per intended requirement. It must be noted that the predicted pressure was very close to the actual gas pressure measured by the gas pressure sensor after 500 cycles. A very small deviation was seen in the maximum predicted gas pressure and the maximum actual gas pressure obtained from the gas pressure sensor.

Figure 4.21 shows both the normalized predicted pressure for both Cell 2 and Cell 3 in the same graph for a better comparison

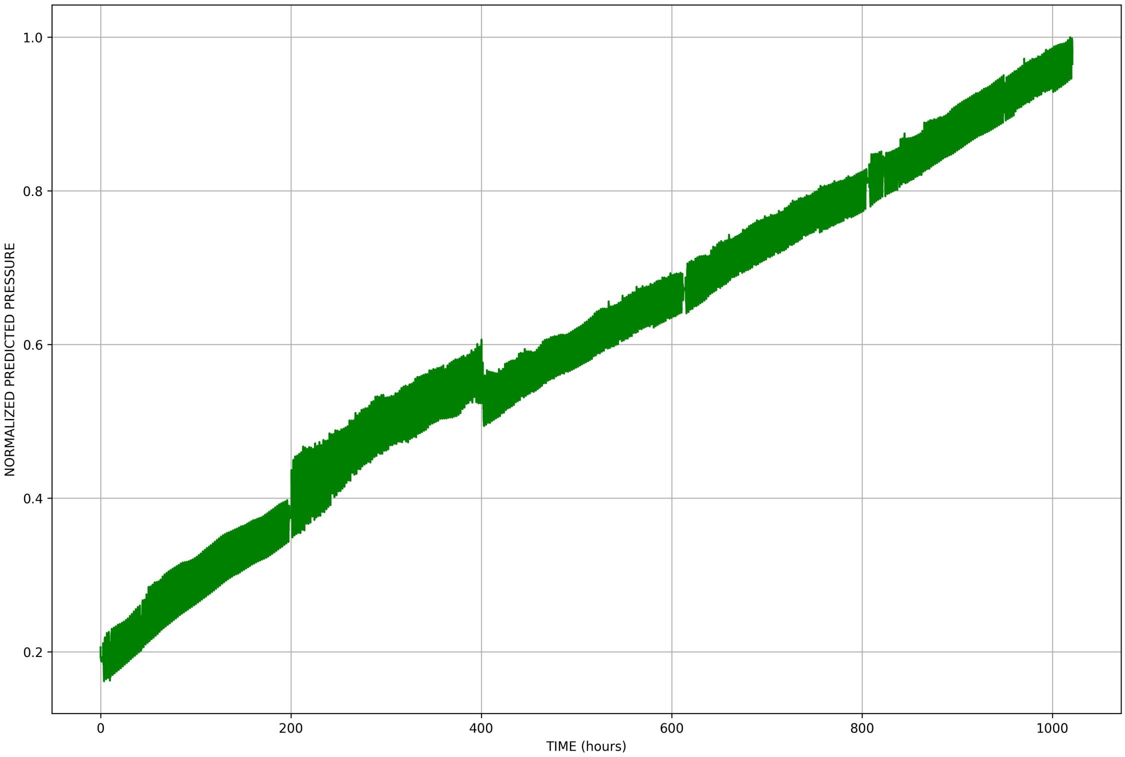

Figure 4.17: Plot of Normalized Predicted Pressure v/s Time : Cell 2 (500 Cycles)

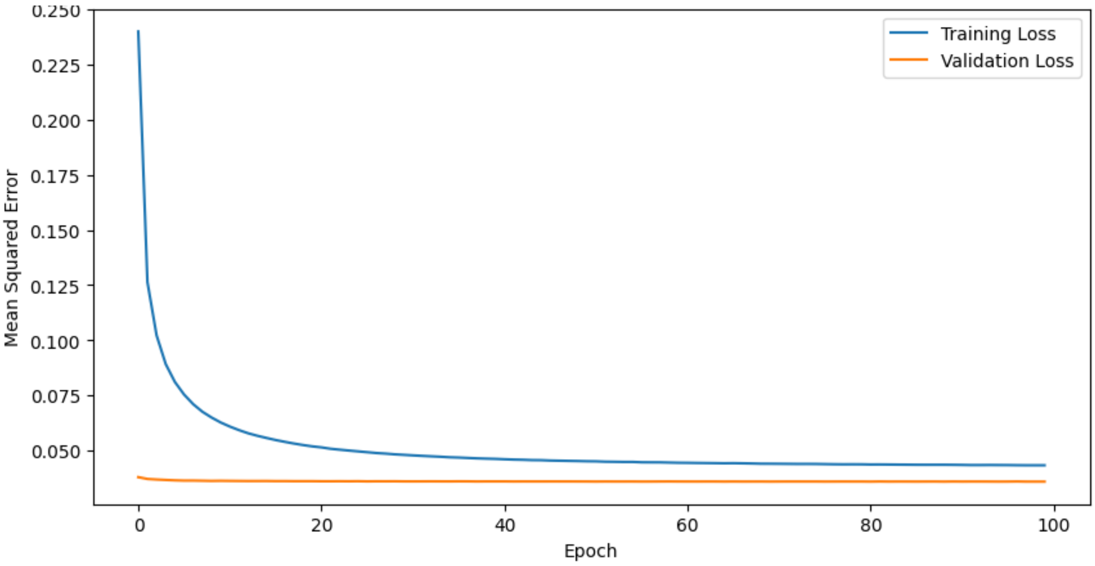

Figure 4.18: Plot of Training Loss and Validation Loss v/s Number of Epochs - Cell 2

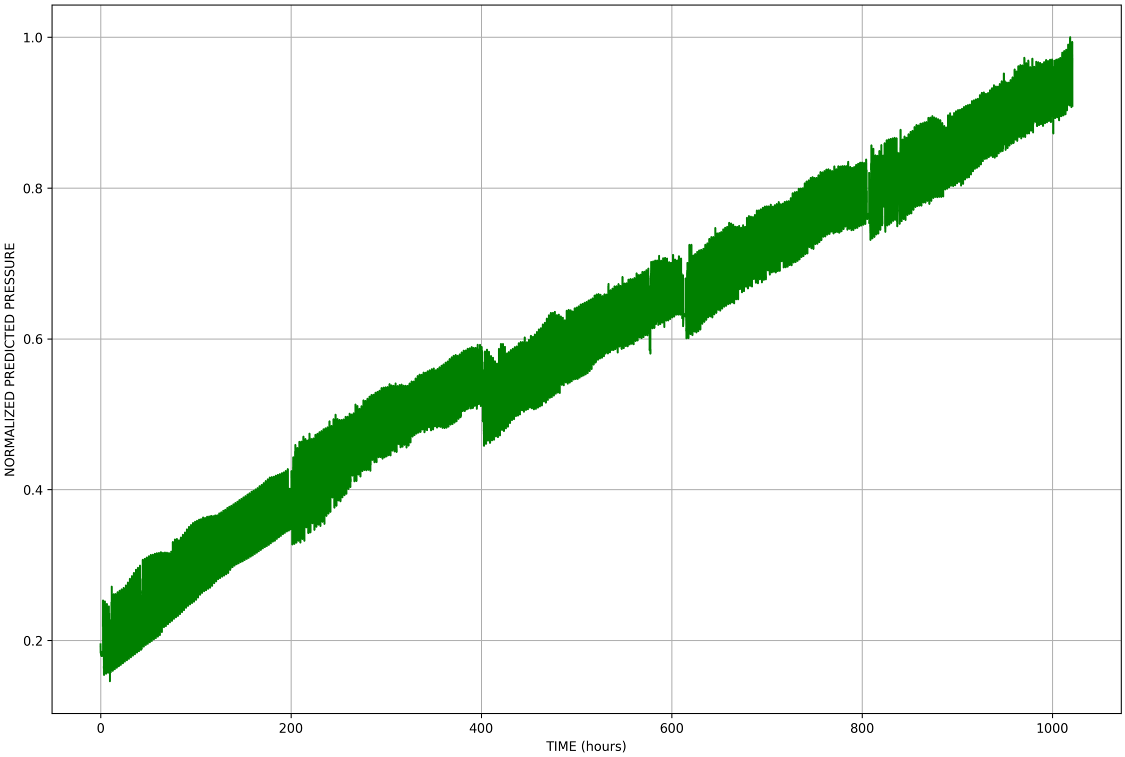

Figure 4.19: Plot of Normalized Predicted Pressure v/s Time : Cell 3 (500 Cycles)

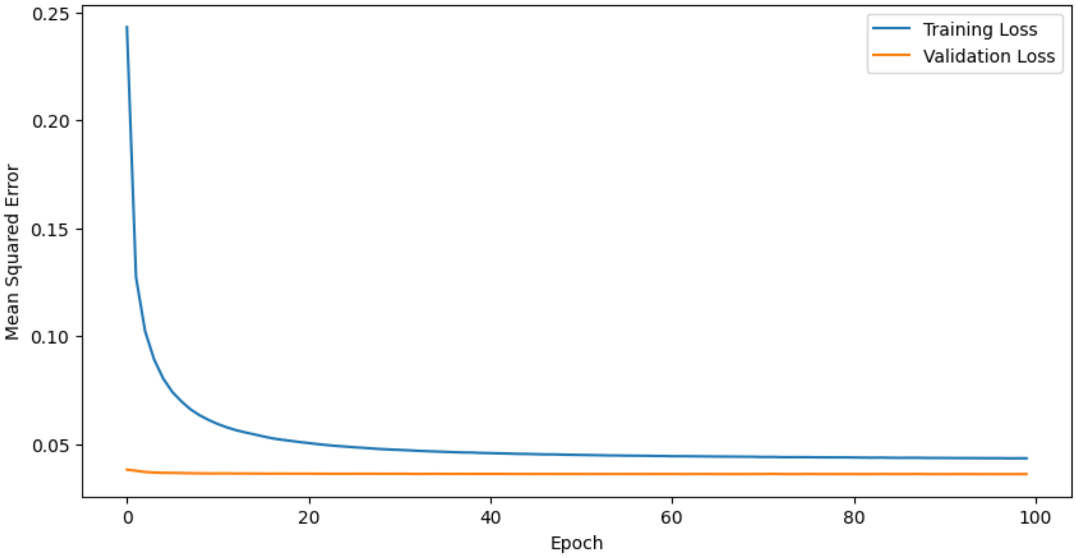

Figure 4.20: Plot of Training Loss and Validation Loss v/s Number of Epochs - Cell 3

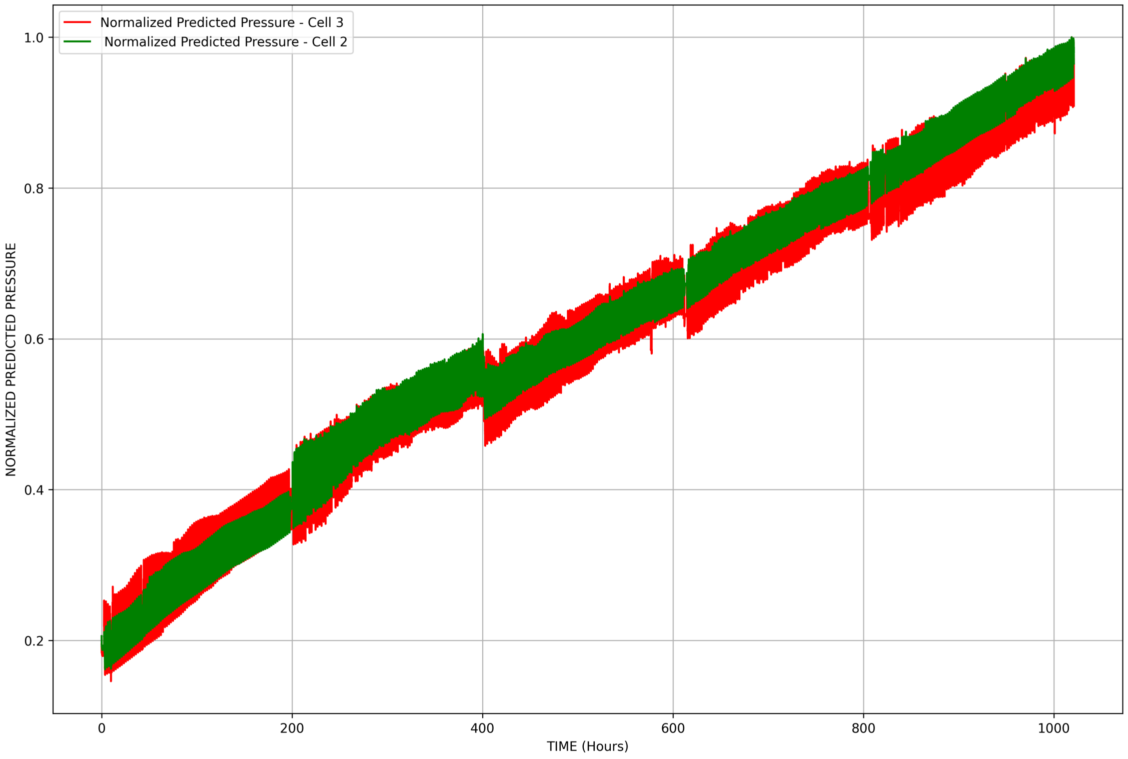

Figure 4.21: Plot of Normalized Predicted Pressure (Cell 2 & Cell 3 v/s Time of an Active Cell (500 Cycles)

4.4 Active Cell Strain - SoH Prediction

Existing BMSs, estimate the health of the battery using conventional electrical data like voltage, current and cell surface temperature. In this study we aim to improve the accuracy of the BMS by complementing the electrical parameters with mechanical parameters that help provide a better picture of the battery condition. With the successful prediction of internal gas pressure of the cell, we now aim to establish a relationship between internal gas pressure of the cell and health of the battery. We know that as the cell cycles over its lifetime, the cell starts aging. This results in the generation of gases inside the cell. As the cell ages, gas generation increases, the DCIR of the cell correspondingly increases and the capacity of the battery gradually starts to decrease. Since we were able to establish a linear correlation between the strain data and the gas pressure data, resulting in a successful prediction of gas pressure using the DNN model, we aim to determine the relationship between the gas pressure and certain health indicators of the battery along with the SoH of the battery.

For this purpose, we selected 3 health indicators that we could use to determine the battery degradation and establish a correlation between the internal gas pressure of the cell and the health indicators. The Health indicators selected were:

- DCIR (80% SoC, 50% SoC & 20% SoC)
- Discharge Energy
- Charge Capacity

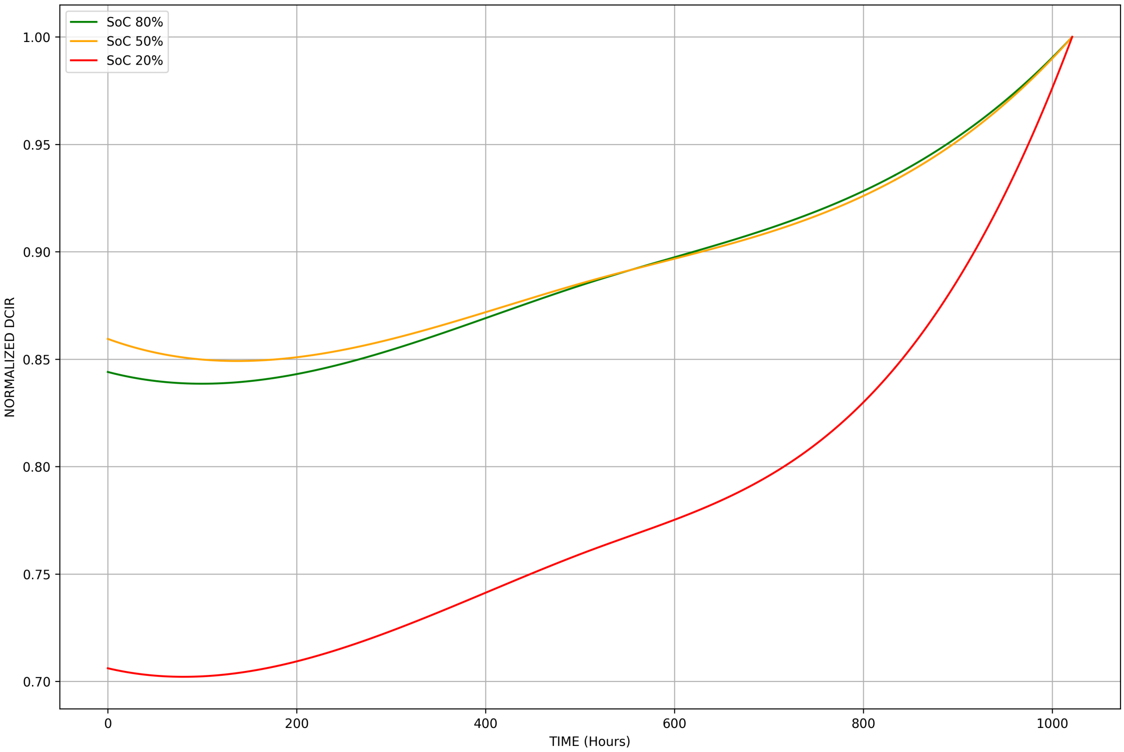

Figure 4.22: Plot of Normalized Predicted Pressure v/s Time of an Active Cell (500 Cycles)

Figure 4.22, depicts the normalized the DCIR obtained from the RPT performed after every 100 cycles of cycling (charging-discharging). The DCIR is measured by applying a very high current pulse for a brief duration of 10 seconds. The voltage difference due to the pulse applied is divided by the current value of the pulse to get the DCIR. This DCIR measured is a cumulative of the resistances that arise due to mechanical contacts within the cell (mechanical contact between jelly roll to current collector, current collector to the cell terminals) and the electrical resistance. It is seen from Figure 4.23, that the predicted gas pressure obtained from the DNN model has an almost linear correlation with the DCIR. The Pearson correlation coefficient between the predicted pressure and the DCIR was found to vary between 0.87 - 0.92 (depending on the SoC at which DCIR is measured).

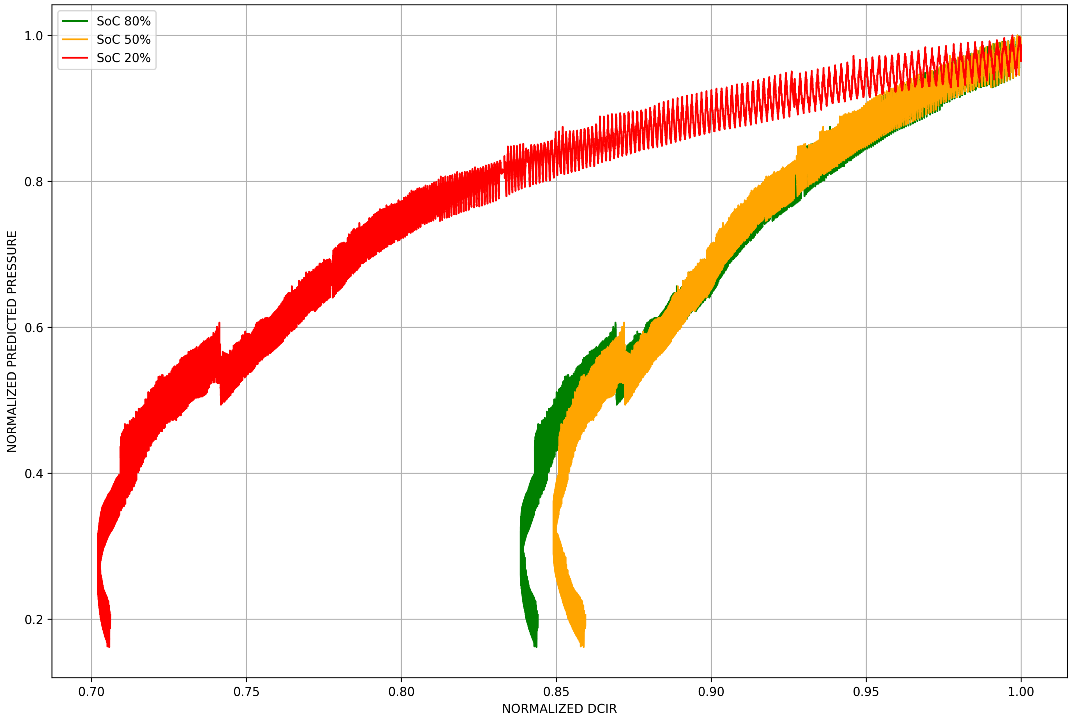

Figure 4.23: Plot of Normalized Predicted Pressure v/s Normalized DCIR (500 Cycles)

The discharge energy of a lithium-ion battery refers to the amount of energy the battery can deliver during a discharge cycle. It is the energy stored in the battery that is released when it powers a device. The normalized discharge energy of the cell under investigation is shown in Figure 4.24. As the cell undergoes cycling, the discharge energy of the cell exhibits a negative linear behaviour, i.e., the discharge energy of the cell decreases with time. As discussed earlier, the internal gas pressure inside the cell (predicted pressure) increases with time and has an almost positive linear trend with the passage of time (as number of cycles increase). When the Predicted Pressure was plotted against the Discharge energy, it was observed that the predicted gas pressure has a negatively linear relationship with discharge energy. As the internal gas pressure increases, the discharge energy of the cell decreases as seen in Figure 4.25.

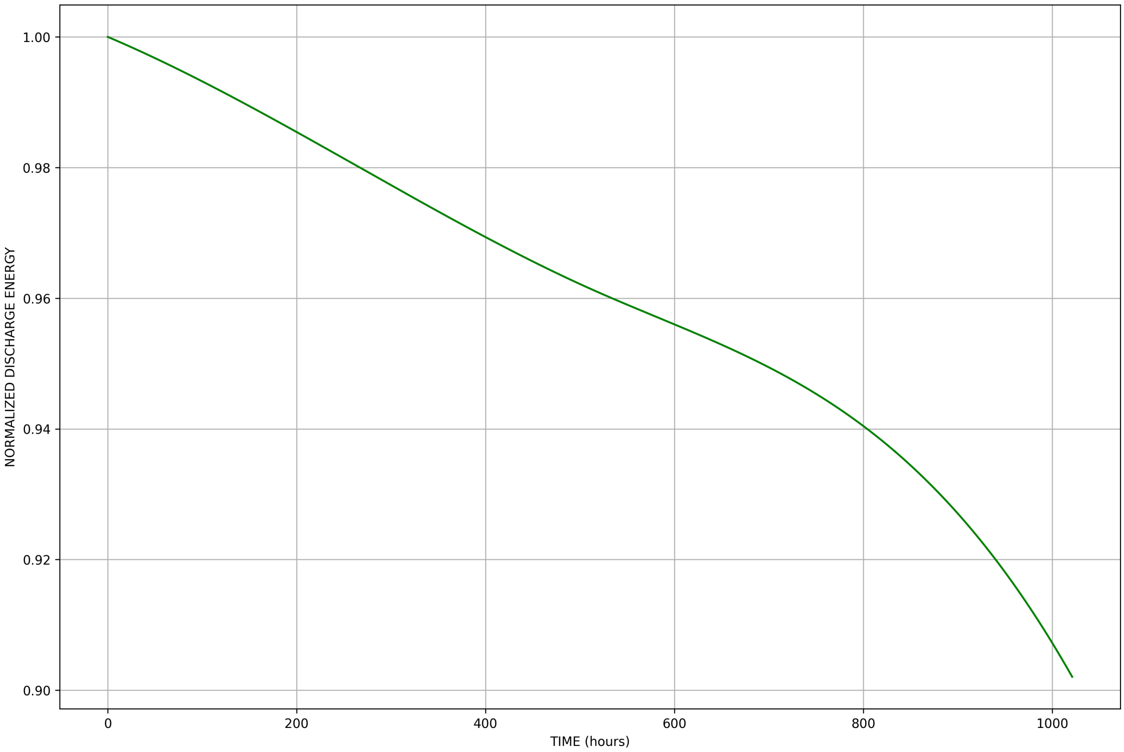

Figure 4.24: Plot of Normalized Discharge Energy v/s Time (500 Cycles)

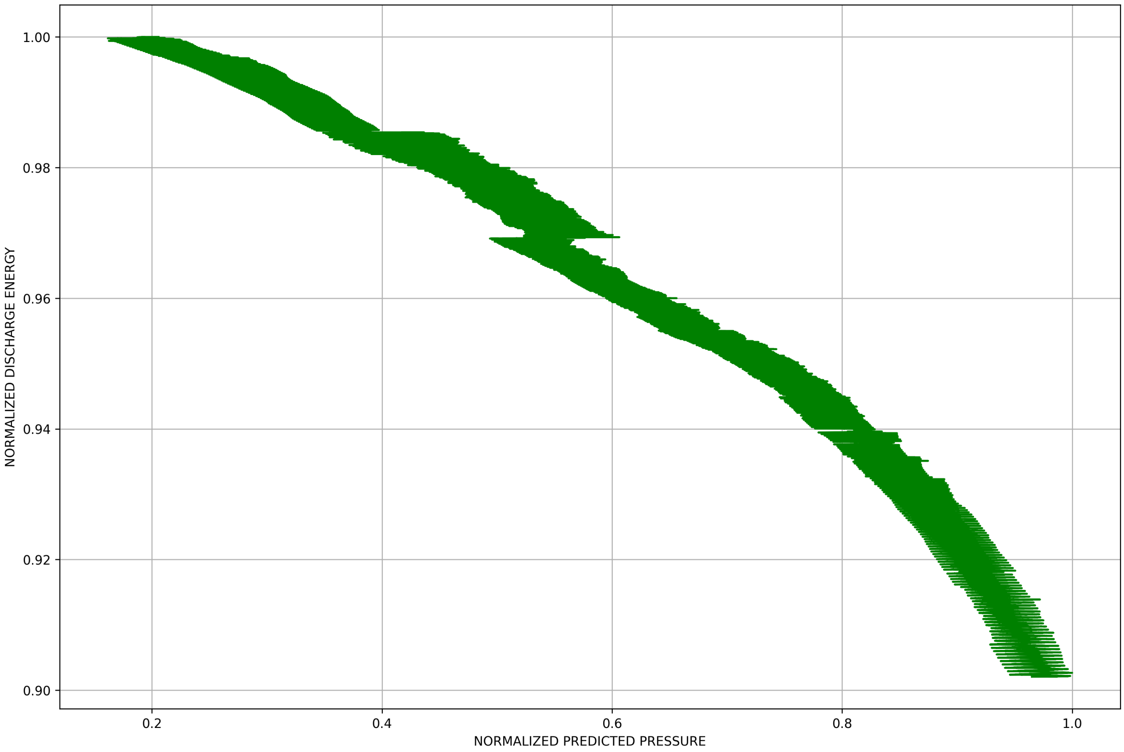

Figure 4.25: Plot of Normalized Discharge Energy v/s Predicted Pressure (500 Cycles)

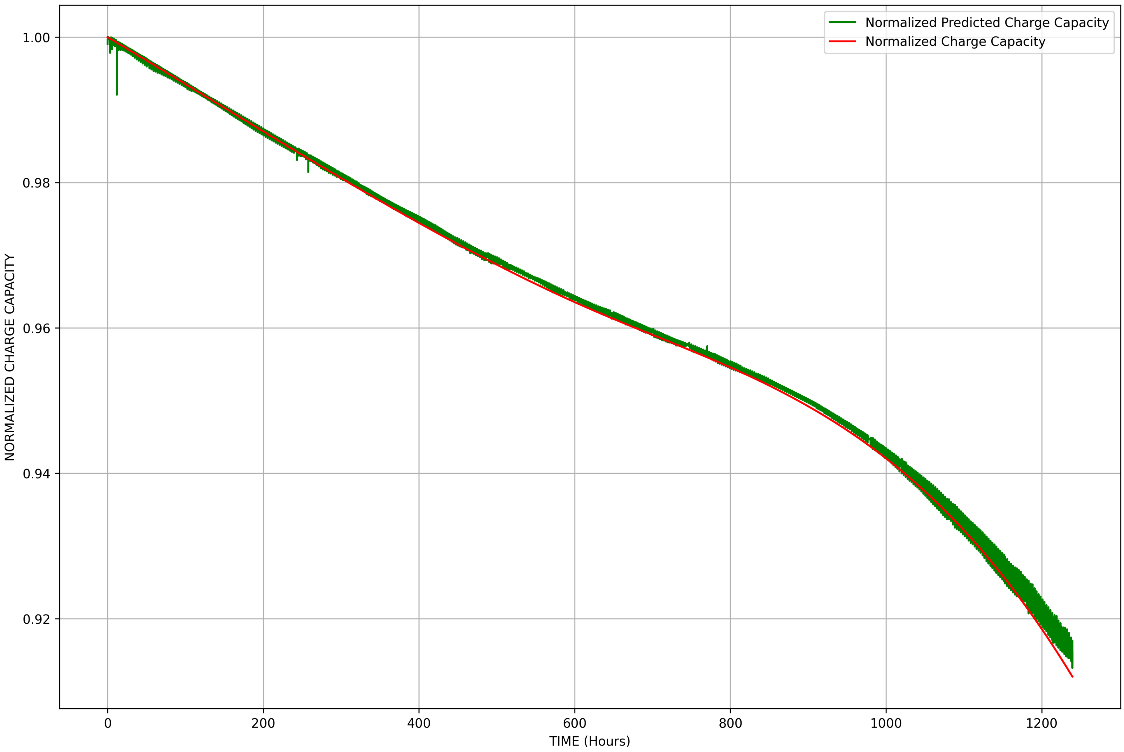

Figure 4.26: Plot of Normalized Predicted Pressure v/s Time of an Active Cell (500 Cycles)

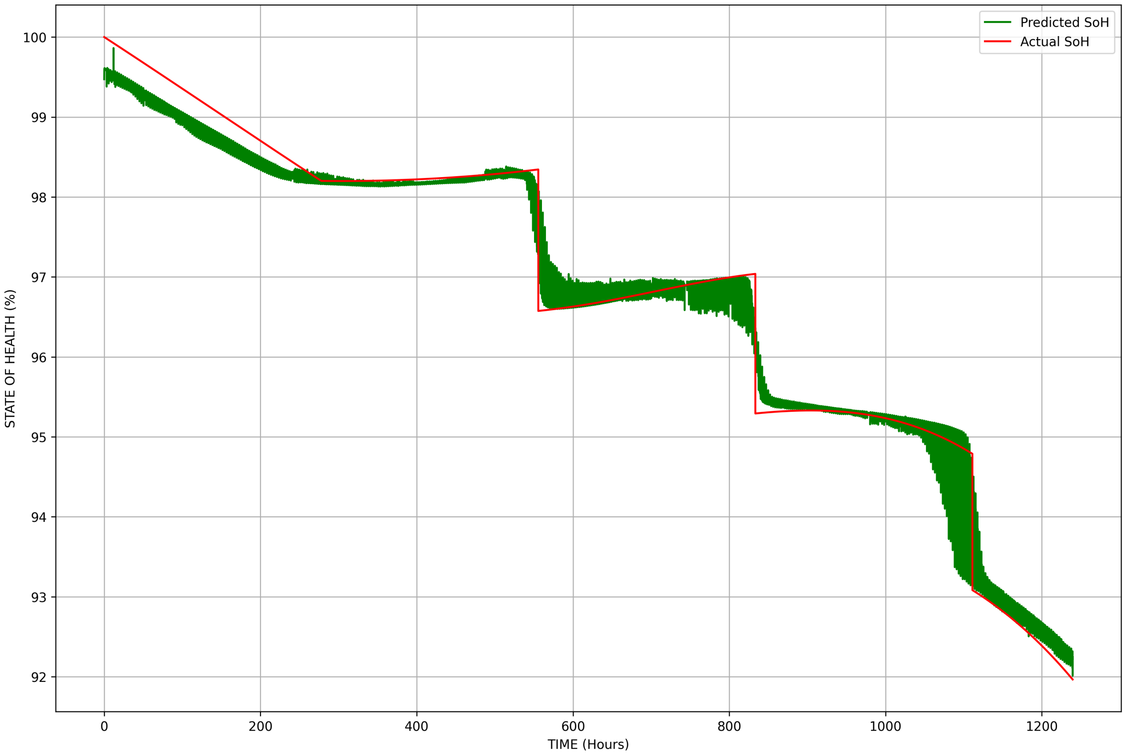

Figure 4.27: Plot of Normalized Predicted Pressure v/s Time of an Active Cell (500 Cycles)

The final health indicator that we selected was the Charge capacity of the cell. The charge capacity of the cell can be used to determine the SoH of the battery in %. Using the charge capacity values, we calculated the SoH. The SoH was calculated using,

$$\text{SoH} = \frac{\text{Current Capacity}}{\text{Rated Capacity}} \times 100 \tag{4.1}$$

where:

- Current Capacity indicates the capacity of the battery at the time of measurement,
- Rated Capacity indicates the initial/original capacity of the fresh cell.

The charge capacity values obtained from the battery cycler were used to calculate the SoH of the battery. The measured capacity and calculated SoH values were then provided as target variables to the DNN for training to make predictions. The 4 input parameters as shown in Table 3.2 were used to train the DNN along with charge capacity and SoH as the two target variables. The results obtained after using the DNN model for the Charge Capacity prediction and SoH prediction are shown in Figure 4.26 and Figure 4.27 respectively. The data represented in the red colour is the true/actual data and the data represented in the green is predicted data. A very close convergence was seen between the actual charge capacity, SoH values and the predicted charge capacity and predicted SoH values as shown in the above mentioned figures. The accuracy of the prediction made by the DNN in estimating the charge capacity and SoH was almost precise and exhibited good accuracy. A statistical analysis was done to compare the actual charge capacity and SoH with the predicted charge capacity and predicted SoH respectively. The statistical metrics can be seen in the Table 4.2 and Table 4.3.

Table 4.2: Statistical Analysis of Charge Capacity and Predicted Charge Capacity

Statistic	**Charge Capacity**	**Predicted Charge Capacity**
Mean	0.991006	0.991097
Standard Deviation	0.0052	0.0050
T-statistic	-12.5507	
P-value	0.0	
Correlation	0.9998	

Table 4.3: Statistical Analysis of SoH and Predicted SoH

Statistic	**SoH (%)**	**Predicted SoH (%)**
Mean	99.1006	98.8139
Standard Deviation	0.5209	0.4417
T-statistic	419.7467	
P-value	0.0	
Correlation	0.9948	

Analysis of the results reveals that the datasets—both measured and predicted—show similar means and variability for charge capacity and State of Health (SoH). Despite the small difference in means, the t-test identifies this difference as statistically significant. This significance is likely attributed to the low variability and large sample size. The correlation between the actual and predicted values for charge capacity and SoH is nearly 1, indicating a very strong positive relationship. The statistical results presented in the table suggests that the values in the predicted dataset are almost linearly related to those in the actual dataset, implying that the two datasets likely exhibit nearly identical trends.

5

Conclusion

The focus of this thesis was to understand the battery condition using mechanical parameters like gas pressure and temperature, in order to compliment the state estimation done by conventional BMS unit where only electrical parameters and surface temperature of the cell are taken into consideration.

5.1 Present Work

The mechanical behaviour of the cell body was studied and we identified that there is a huge knowledge gap in the existing research with regards to the gas generation inside cells and their measurement techniques. Non-invasive gas pressure measurement was one of the main focus points of this thesis. A new method was developed where with the help of strain gauges, we were able to capture the response behaviour of the battery to changing internal gas pressure. DNN models were used to successfully predict the internal gas pressure inside the cell. A correlation was established between the strain developed in the lid of the cell and the gas pressure developed inside the cell. There exists an almost perfectly linear relationship between the internal gas pressure and the strain developed on the cell lid.

We then dived deep into establishing a relationship with gas pressure and the health of the battery. For this, we examined various health indicators that we could employ in determining the SoH of the battery. a successful correlation was established between the strain reading from the lid, the internal gas pressure and the charge capacity of the cell. DCIR and discharge energy can also be used as health indicators to determine the battery health using gas pressure data and a DNN model.

5.2 Future Work

The new method developed in predicting internal gas pressure and predicting the SoH of the battery using gas pressure, can be scaled to the pack level from the cell level and these can be integrated to the real-world BMS for better and accurate state estimation of various parameters of the battery pack. Measurement of strain can be improved by using more advanced technologies like FBG sensor or lasers that monitor the strain developed in the cell during its lifetime. These new-age measurement methods can further improve the state estimation and eliminate noise during data collection and hence produce more accurate predictions.

6

Ethics

The following ethical principles were carefully considered in the execution of this work,

- **Societal Impact**: This work seeks to enhance the understanding of battery performance, health, and real-time state analysis. By monitoring additional parameters, such as the internal gas pressure of the battery, alongside conventional metrics like voltage, current, and surface temperature, the Battery Management System (BMS) can gain a more comprehensive insight into the battery's condition. This improved understanding will enable the development of more effective optimization strategies for battery usage by the BMS. This improved understanding will enable the BMS to implement more effective optimization strategies for battery usage, ultimately increasing the battery pack's life cycle, reducing costs, and providing a safer driving experience through early detection of potential thermal runaway events.

- **Honesty and Integrity**: The research and discussion presented in this thesis are both true and original, with no plagiarism or unauthorized use of others' work. Numerous research papers and journals have been consulted, and all referenced works have been properly cited, with full acknowledgment of their contributions.

- **Confidentiality and Transparency**: Significant effort has been made to clearly present and explain the concepts and results in this thesis, while ensuring that sensitive data is not disclosed. A thorough review was conducted before presenting models, technical specifications, methodology, and results. The methodology and findings have been transparently shared in strict compliance with confidentiality agreements.

7

Sustainability

As the automotive industry transitions towards cleaner and greener energy sources, finding alternatives to conventional internal combustion engine (ICE) vehicles has become critical. Battery-powered vehicles currently stand out as the most viable option, due to their ability to meet or even exceed the performance of ICE technology in terms of both vehicle functionality and environmental impact. Leading OEMs have committed to converting a significant portion of their market share to electric vehicles (EVs) by 2030. To achieve these ambitious targets, it is essential to develop sustainable and environmentally friendly batteries. This can be approached in three key ways: responsibly sourcing raw materials and utilizing eco-friendly extraction methods, reducing pollution in the battery production process, and most importantly, significantly extending the lifespan of batteries to minimize waste. The United Nations' Sustainable Development Goals (SDGs), which address a range of social, economic, and environmental challenges, can serve as a framework for the responsible development of lithium-ion batteries. As a key technology in energy storage, electric vehicles, and portable electronics, lithium-ion batteries align with several SDGs, particularly SDG 7 (Affordable and Clean Energy), SDG 9 (Industry, Innovation, and Infrastructure), and SDG 11 (Sustainable Cities and Communities).

The research and study conducted in this work align with the aforementioned SDGs and their objectives. The affordability of batteries and electric vehicles (EVs) can be improved through innovative techniques in Battery Management Systems (BMS). By incorporating modern BMS technologies and optimization algorithms, and considering additional battery parameters such as internal gas pressure alongside conventional parameters like voltage, current, and cell surface temperature, we can enhance battery pack utilization. This approach extends the useful life of batteries, reduces battery waste, and addresses the challenge of limited battery cycle life. The work discussed is not only restricted to the prismatic Li-ion batteries. This can be extended to different formats of the Li-ion batteries (cylindrical & pouch cells) and other potential chemistry like Sodium-ion batteries.

Bibliography

[1] S&P Global Report on EV Adoption,
`https://www.spglobal.com/en/research-insights/featured/special-editorial/look-forward/the-journey-to-further-ev-adoption`

[2] Global EV Outlook 2024,
`https://iea.blob.core.windows.net/assets/aa21aa97-eea2-45b4-8686-ae19d8939161/GlobalEVOutlook2024.pdf`

[3] Review of gas emissions from lithium-ion battery thermal runaway failure — Considering toxic and flammable compounds,
`https://doi.org/10.1016/j.est.2024.111288`

[4] Lithium loss, resistance growth, electrode expansion, gas evolution, and Li plating: Analyzing performance and failure of commercial large-format NMC-Gr lithium-ion pouch cells,
`https://doi.org/10.1016/j.jpowsour.2024.234494`

[5] Graphite lithiation and capacity fade monitoring of lithium ion batteries using optical fibers,
`https://doi.org/10.1016/j.est.2020.101233`

[6] Lithium-Ion Battery State of Charge (SoC) Estimation with Non-Electrical parameter using Uniform Fiber Bragg Grating (FBG),
`https://doi.org/10.1016/j.est.2021.102704`

[7] Nonintrusive Fiber Optic LIB Inner Gas Pressure Sensor Based on Characteristic Frequency Shift

[8] M. Klett et al., “Non-uniform aging of cycled commercial LiFePO4//graphite cylindrical cells revealed by post-mortem analysis,” J. Power Sources, vol. 257, pp. 126–137, Jul. 2014,
`https://doi:10.1016/j.jpowsour.2014.01.105`

[9] Health indicator selection for state of health estimation of second-life lithium-ion batteries under extended ageing,
`https://doi.org/10.1016/j.est.2022.105366`

[10] A new state-of-health estimation method for lithium-ion batteries through the intrinsic relationship between ohmic internal resistance and capacity,
`https://doi.org/10.1016/j.measurement.2017.11.016`

[11] In-situ measurement of internal gas pressure within cylindrical lithium-ion cells,
`https://doi.org/10.1016/j.jpowsour.2023.233064`

[12] Effects of charging rates on heat and gas generation in lithium-ion battery thermal runaway triggered by high temperature coupled with overcharge,
`https://doi.org/10.1016/j.jpowsour.2024.234237`

[13] Lithium-Ion Batteries: Basics and Applications,
`https://doi.org/10.1007/978-3-662-53071-9`

[14] Battery Management Systems, Battery Modelling - Gregory L. Plett,
`ISBN-13:978-1-63081-023-8`

[15] Direct venting during fast charging of lithium-ion batteries,
`https://doi.org/10.1016/j.jpowsour.2023.233926`

[16] Measurement of gas pressure inside large-format prismatic lithium-ion cells during operation and cycle aging,
`https://doi.org/10.1016/j.jpowsour.2020.228661`

[17] Study of the influence of mechanical pressure on the performance and aging of Lithium-ion battery cells,
`https://doi.org/10.1016/j.jpowsour.2019.227148`

[18] In operando measurement of surface strain of 18650 Li-ion cells,
`https://doi.org/10.1016/j.jpowsour.2023.233915`

DEPARTMENT OF ELECTRICAL ENGINEERING
CHALMERS UNIVERSITY OF TECHNOLOGY
Gothenburg, Sweden
www.chalmers.se

CHALMERS
UNIVERSITY OF TECHNOLOGY